Geochemistry, Geophysics, Geosystems®

AGU ADVANCING EARTH AND SPACE SCIENCE

RESEARCH ARTICLE
10.1029/2021GC010260

Dyke Architecture, Mineral Layering, and Magmatic Convection; New Perspectives From the Younger Giant Dyke Complex, S Greenland

L. Koopmans[1,2], W. McCarthy[1], and C. Magee[3]

[1]School of Earth & Environmental Sciences, University of St Andrews, St Andrews, UK, [2]Department of Earth Sciences, University of Oxford, Oxford, UK, [3]Institute of Geophysics and Tectonics, School of Earth Science and Environment, University of Leeds, Leeds, UK

Key Points:

- The Younger Giant Dyke Complex (<800 m wide, 150 km long), S Greenland was emplaced as a series of isolated segments
- Petrography and anisotropy of magnetic susceptibility fabrics identify segments behaved independently, even after segments coalesced
- Igneous layering formed through hydrodynamic processes at the magma-mush boundary, and crystallization occurred in a convecting system

Supporting Information:

Supporting Information may be found in the online version of this article.

***Correspondence to:**

L. Koopmans,
lot.koopmans@univ.ox.ac.uk

Citation:

Koopmans, L., McCarthy, W., & Magee, C. (2022). Dyke architecture, mineral layering, and magmatic convection; new perspectives from the Younger Giant Dyke Complex, S Greenland. *Geochemistry, Geophysics, Geosystems*, *23*, e2021GC010260. https://doi.org/10.1029/2021GC010260

Received 10 NOV 2021
Accepted 14 FEB 2022

Author Contributions:

Conceptualization: L. Koopmans, W. McCarthy, C. Magee
Data curation: L. Koopmans
Formal analysis: L. Koopmans
Funding acquisition: L. Koopmans, W. McCarthy
Investigation: L. Koopmans
Methodology: L. Koopmans, W. McCarthy
Supervision: W. McCarthy, C. Magee
Validation: W. McCarthy, C. Magee

Abstract Igneous sheet intrusions are a fundamental component of volcano plumbing systems. Identifying how sheet intrusion emplacement and geometry controls later magmatic processes is critical to understanding the distribution of volcanic eruptions and magma-related ore deposits. Using the Younger Giant Dyke Complex (YGDC), a Mesoproterozoic suite of large (<800 m wide) mafic dykes in southern Greenland, we assess the influence sheet of emplacement and geometry on subsequent magma flow and mush evolution. Through structural mapping, petrographic observations, and anisotropy of magnetic susceptibility fabric analyses, we show that the YGDC was emplaced as a series of individual dyke segments, which following coalescence into a sheet intrusion remained largely isolated during their magmatic evolution. Through petrographic evidence for liquid-rich growth of cumulus phases, concentric magnetic fabrics, and the detailed study layered zones within the YGDC, we infer magma convection occurred within the cores of each dyke element. We particularly relate layering to hydrodynamic sorting processes at a magma-mush boundary toward the base of each convection cell. Overall, our work demonstrates that the initial geometry of sheet intrusions can constrain magma flow patterns and affect the distribution of crystallization regimes.

1. Introduction

Deciphering interactions between magma emplacement, magma flow, and crystallization processes in igneous intrusions are critical to understanding the evolution of volcanic systems (Cashman et al., 2013). For example, magma emplacement style dictates the initial geometry of intrusions, which can impart a structural control on the subsequent distribution of eruptions and crystallization processes (Cashman et al., 2013; Maes et al., 2007; McBirney & Nicolas, 1997; Schofield, Heaton, et al., 2012). Layered sheet intrusions are particularly useful for unraveling how syn- and post-emplacement magmatic processes interact, because their external geometries are relatively simple and the layering they contain provides a quantifiable record of crystallization (Irvine, 1980; McBirney & Nicolas, 1997; O'Driscoll et al., 2015; Selkin et al., 2014; Tex, 1969). Various studies have shown layering within sheet intrusions can form through both emplacement (e.g., Ferré & Marsh, 2002; Maes et al., 2007) and later cumulus processes (e.g., McBirney & Nicolas, 1997; O'Driscoll et al., 2007; Selkin et al., 2014); they therefore provide key insight into the relationship between emplacement and crystallization.

A growing body of research has shown that sheet intrusions are commonly emplaced as a series of isolated elements (e.g., segments and magma fingers, Figure 1), which eventually coalesce to form a continuous sheet as further magma input and element inflation occurs (Healy et al., 2018; Hutton, 2009; Magee, Muirhead, Schofiled, et al., 2016; Magee, Muirhead, Karvelas, et al., 2016; Nicholson & Pollard, 1985; Schofield, Heaton, et al., 2012). The formation and coalescence of such elements has been shown to play a major role in the (re)direction and channelization of magma flow, and thus compartmentalization of sheet intrusions, during their evolution (Figure 1) (e.g., Ferré & Marsh, 2002; Holness & Humphreys, 2003; Maes et al., 2007; Martin et al., 2019; Schofield, Brown, et al., 2012). Although several studies have considered how the formation of segments within sheet intrusion affects magma flow, few have considered how their presence impacts post-emplacement convection and crystallization processes (Figure 1) (Magee et al., 2013; Magee, O'Driscoll, et al., 2016).

To examine interactions between emplacement and later crystallization processes in layered intrusions, detailed petrographic and structural studies are required (Holness, Farr, et al., 2017; Holness & Humphreys, 2003; McBirney & Nicolas, 1997; O'Driscoll et al., 2015). In particular, petrofabric analyses are critical because the

Visualization: L. Koopmans
Writing – original draft: L. Koopmans, W. McCarthy, C. Magee
Writing – review & editing: L. Koopmans, W. McCarthy, C. Magee

alignment of crystals they record enables a quantitative assessment of the distribution of strain in igneous rocks, which can be attributed to various magmatic and post-magmatic processes (e.g., Ferré & Marsh, 2002; Holness & Humphreys, 2003; McBirney & Nicolas, 1997; McCarthy et al., 2015). However, magmatic fabrics, such as mineral lineations, are often weak and time-consuming to measure in the field (if they are visible) or laboratory (Higgins, 2006). To overcome these limitations of petrofabric analyses, many studies use anisotropy of magnetic susceptibility (AMS) as a means to quantify large amounts of magnetic fabrics in a quick, non-destructive manner (Borradaile & Jackson, 2004; Cheadle & Gee, 2017; O'Driscoll et al., 2015). By adequately characterizing the origin of AMS in rocks, AMS can be linked to true petrographic fabrics formed through different magmatic processes (e.g., Ferré & Marsh, 2002; Knight & Walker, 1988; O'Driscoll et al., 2015; Selkin et al., 2014). AMS has therefore been used in several studies to decipher the interaction between emplacement geometries and subsequent magmatic processes in many horizontal intrusions (e.g., Martin et al., 2019; O'Driscoll et al., 2015). Although dykes are often too thin for detailed AMS analyses of internal magmatic processes (Holness, Neufeld, et al., 2017), the Younger Giant Dyke Complex (YGDC) in Southern Greenland comprises a suite of excellently exposed, up to 800 m wide dykes that contain regions of igneous layering, foliations, and/or differentiated lithologies (Figure 2) (Koopmans et al., 2021; Upton, 2013); the YGDC thus provides a unique opportunity to study emplacement and magmatic processes in dykes (Upton, 2013). Igneous layering in the YGDC occurs concomitant with a well-developed foliation within wider zones of the dyke system, with each layered zone defining a bowl-shaped morphology. This study aims to constrain the relationship between emplacement and magmatic processes in dykes, and to understand what processes drove the development of igneous layering in wide sections of the YGDC. Through field, petrographic, and magnetic analyses, we find that the YGDC was emplaced as a set of individual segments that subsequently coalesced. The original segmented emplacement of the YGDC created a set of isolated convective magma systems, which inhibited the propagation of the solidification front inwards, separating the margins from the core of each element and isolating them from each other for the majority of the YGDC magmatic history. We show that layering most likely occurred at the magma-mush boundary at the base of these convective cells in response to crystal deposition at the turbulent boundary layer. Overall, our work demonstrates that the initial geometries of sheet intrusions may play a critical role in the evolution of the magma system by affecting magma flow patterns and the distribution of crystallization regimes.

2. Background Geology

The Mesoproterozoic (1,163 ± 2 Ma) YGDC is part of the Gardar Igneous Province in Southern Greenland, which developed along two parallel ENE-trending rift zones that cross-cut the Ketilidian terrane (Figure 2a) (Upton, 2013). The Ketilidian terrane is typified here by the large, calc-alkaline, Julianehåb Batholith, which was emplaced during the Ketilidian orogeny (1855–1795 Ma; Chadwick et al., 1994; Garde et al., 2002; Van Kranendonk et al., 1993). Other components of the voluminous alkaline magmatism that formed the Gardar Igneous Province include giant dyke swarms (the Older Giant Dyke Complex and Late Gardar Swarm), diatremes, and large evolved layered intrusions such as the Illimaussaq and Motzfeld complexes (Figure 2a) (Upton, 2013; Upton & Emeleus, 1987; Upton et al., 2003). Extensional tectonics, deposition of terrestrial sandstones, and extrusive lava flows associated with the Gardar Igneous Province are interpreted to have occurred during the break-up of the Columbia supercontinent (1300–140 Ma; Upton, 2013). Subsequent erosion, block faulting, and uplift has exhumed rocks that were at 3–5 km depth during intrusion of the YGDC to the surface (Andersen, 1997). Notably, the Gardar Igneous Province has undergone no regional metamorphism, and thus preserves a pristine magmatic record from a deep time tectonic event (Upton, 2013; Upton & Emeleus, 1987; Upton et al., 2003).

3. Methods

3.1. Sampling

To examine how fabrics vary across the different lithologies of the YGDC, orientated block samples were collected during a 6-week mapping expedition to Tuttutooq in 2019. Sampling was focused along six transects in the well-exposed southern sheet of the YGDC, and designed to intersect different aspects of the dyke including the layered pods and areas where the intrusion narrows to <150 m thick (Figure 3). Four transects (T1–T4) were oriented North-South, perpendicular to the strike of the dyke, and an additional two transects (T5 and T6) were taken parallel to the strike of the dyke across a well exposed layered zone in the YGDC (Figure 3). Transects were collected along coastal sections (where available) or regions with the most continuous exposures (Figure 3). At

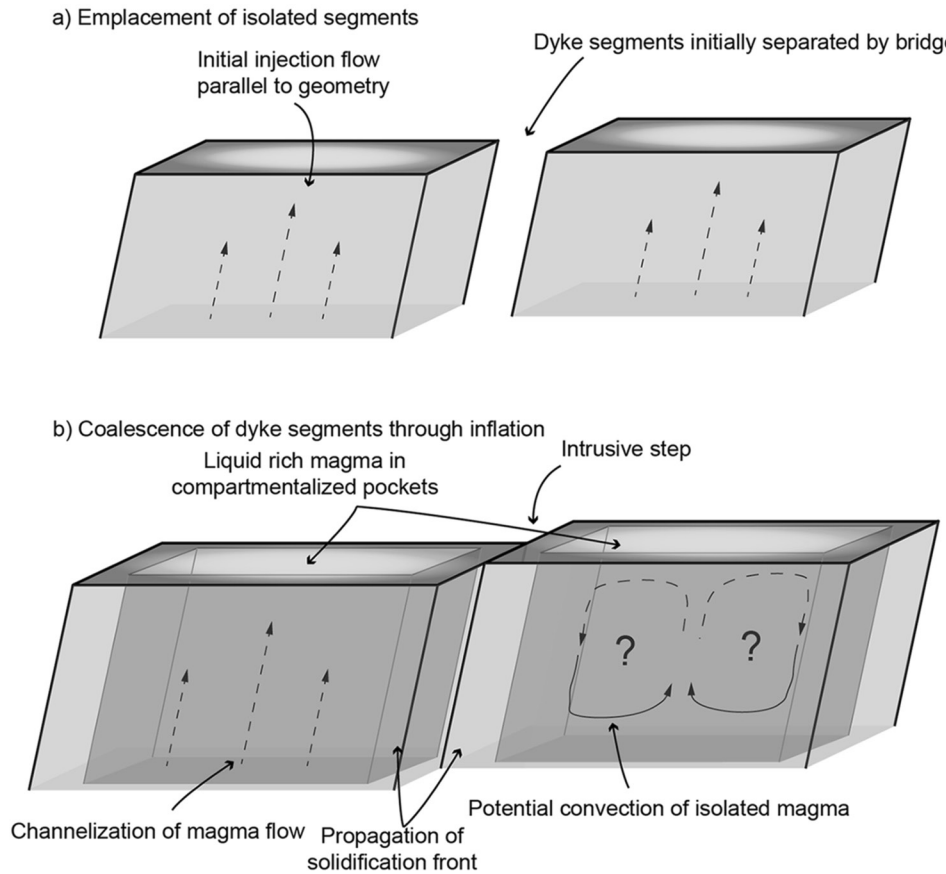

Figure 1. Schematic diagram of a vertical intrusion with individual dyke elements. (a) Initial emplacement of isolated segments with injection flow parallel to the geometry of the segments. (b) Further inflation of individual dyke segments lead to the formation of a single intrusion. The segments in this sketch represent different possible post-emplacement processes. Continued propagation of solidification fronts can lead to liquid rich magma becoming compartmentalized in isolated pockets which subsequently behave independently. The left dyke element represent the possible channelization of magma flow along the core of the intrusion. The right dyke element represents the possible convective magma flow that may occur within isolated elements of an intrusion.

every tenth sample site a duplicate sample was collected to assess within-locality consistency. Sample locations were mapped using a GPS. Standard 25×21 mm cylindrical cores were prepared using a non-magnetic diamond-tipped drill bit and saw at the University of St. Andrews. A total of 13 polished thin sections oriented perpendicular to AMS foliation, taking care to incorporate key observable structures, were prepared from representative sub-specimens to study silicate and oxide mineral textural relationships and assess microstructural properties of petrographic fabrics.

3.2. Rock Magnetic Analyses

3.2.1. Rationale

Anisotropy of magnetic susceptibility (AMS) is based on the principle that most minerals in a sample are easier (susceptible) to magnetize along preferred axes controlled by either the crystallographic orientation (i.e., for paramagnetic crystals) or grain-shape anisotropy (i.e., for ferromagnetic crystals) (Borradaile & Jackson, 2004). By measuring a samples susceptibility to magnetization within a variably oriented, external magnetic field, we can thus quantify fabrics related to the orientation, distribution, and chemistry of magnetic carriers in various rocks (Borradaile & Jackson, 2004; Tarling & Hrouda, 1993). For example, AMS has been used extensively to study magma propagation directions and emplacement processes as anisotropic crystals often align with the direction of flow; this is particularly valuable in studies of fine grained rocks where conventional methods of identifying

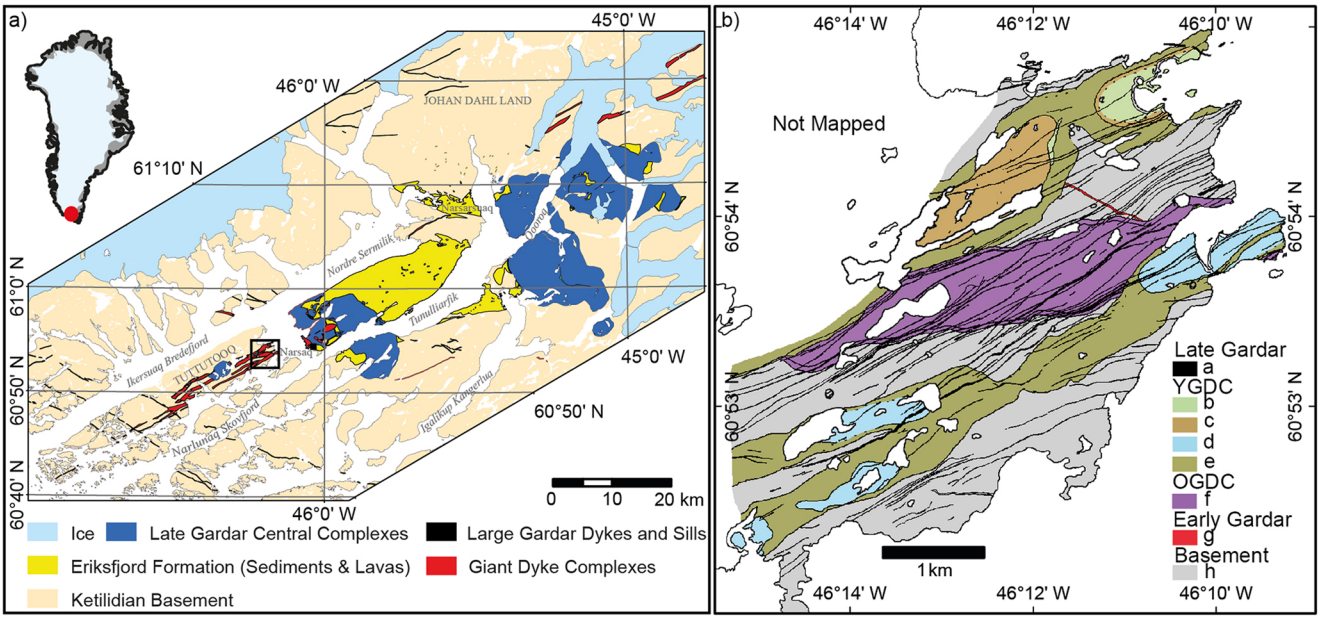

Figure 2. (a) Simplified regional geological map of the Tuttutooq-Illimaussaq-Narsarssuaq rift zone of the Gardar Igneous Province, South Greenland. Location of (b) marked with black square. (b) Simplified geological map of study area (after Koopmans et al., 2021). Units are as follow, (a) Gardar dyke swarm, (b) Alkali feldspar syenite, (c) Syenogabbro, (d) Foliated and/or modally layered troctolite, (e) Troctolite, (f) Older Giant Dyke (syenogabbros and syenites), (g) Gardar brown dykes, (h) Ketilidian Julianehab granite.

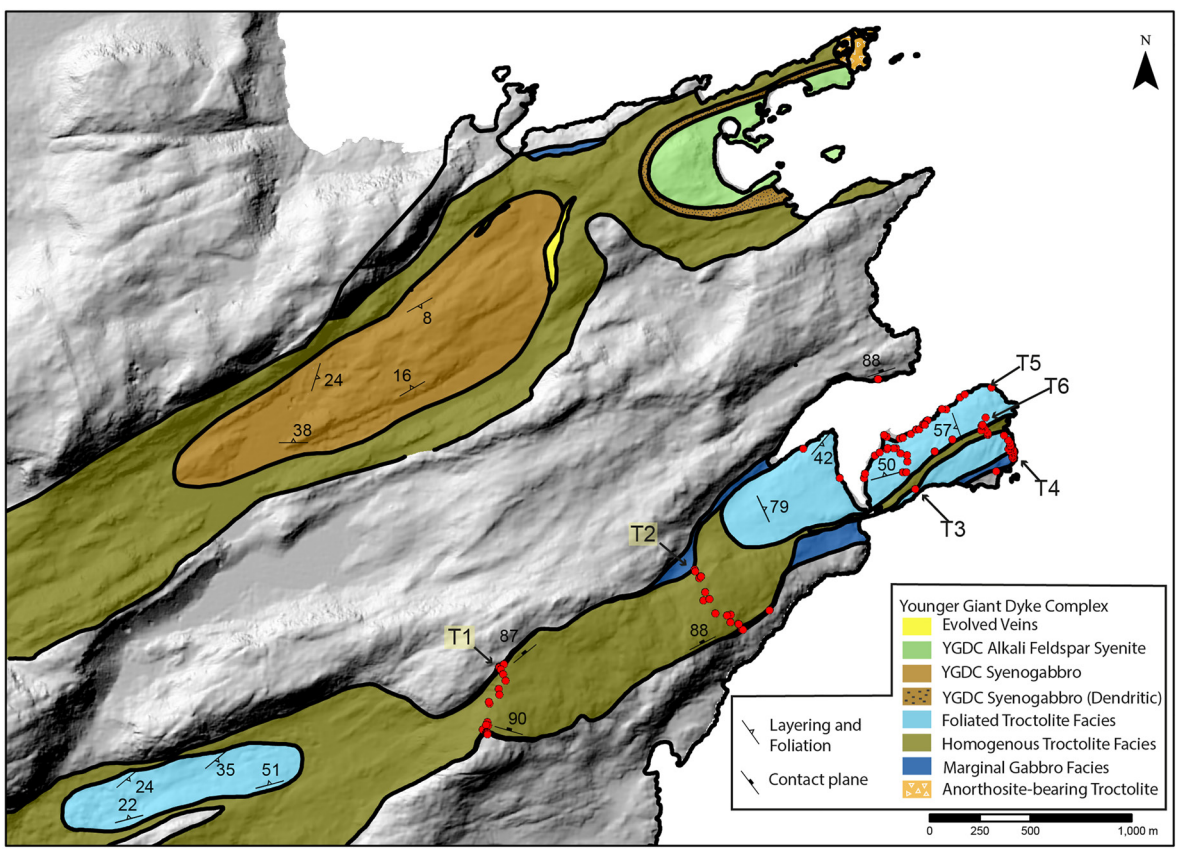

Figure 3. Simplified map of Younger Giant Dyke Complex (YGDC) exposures on Eastern Tuttutooq. Sampled locations marked with red dot, with transect numbers labeled. Descriptions of rock types in northern sheet of the YGDC are provided in Koopmans et al. (2021).

flow directions (e.g., ropy textures, shape preferred orientations, anisotropic vesicles) are difficult to resolve or not present (e.g., Knight & Walker, 1988; Maes et al., 2007; Magee et al., 2012). Similarly, AMS has been used to reliably identify lineations in layered intrusions, providing key insight into the nature of magma flow regimes in large plutons (e.g., Ferré & Marsh, 2002; O'Driscoll et al., 2008, 2015). AMS can therefore provide key insights into the interaction between emplacement geometry and magmatic processes.

It is important to note that the orientation of an AMS response differs between magnetic carriers, as different mineral groups, grain sizes, and mineral orientations relative to the inducing field affects the relationship between the magnetic fabric and the true crystal orientation (Biedermann, 2018; Biedermann et al., 2018; Borradaile & Jackson, 2004; Dunlop & Özdemir, 1997; Khan, 1962; Rochette et al., 1992; Wing-Fatt & Stacey, 1966). Therefore, to determine the validity and significance of an AMS response, it is important to characterize the magnetic phases in a rock. This characterization can be done through various petrographic and magnetic characterization experiments. Petrographic analyses provide qualitative information on present phases which may contribute to the AMS response, but provide little information on the relative contributions to the magnetic susceptibility (Tarling & Hrouda, 1993). Bulk magnetic characterization experiments, such as temperature-susceptibility experiments, can provide a quantitative assessment of the relative contributions of various magnetic phases in a sample to bulk susceptibility, which often correlates to the anisotropic magnetic response of a rock (Dunlop & Özdemir, 1997; Tauxe, 1998). When ferromagnetic grains are shown to dominate the bulk susceptibility response, conducting further magnetic remanence experiments can provide additional information on the grain size of the ferromagnetic population in a sample. Ferromagnetic minerals have characteristic coercivity spectra that are dependent on their chemistry and grain size, which is important to constrain as particular grain sizes have been shown to produce inverse anisotropy responses (e.g., single-domain magnetite) (Dunlop & Özdemir, 1997).By better constraining the magnetic mineralogy, more confidence can be put on the interpretation of the AMS analyses.

3.2.2. Anisotropy of Magnetic Susceptibility Analyses

AMS and bulk susceptibility were measured simultaneously on an AGICO KLY-5A Kappabridge (400 Am^{-1} peak field, 1,220 Hz peak frequency, room temperature) at the M^3Ore lab, University of St Andrews. An average of 13 sub-specimens were collected from each of the 104 sample sites; results are reported as mean AMS tensors averaged across their sub-specimens (normalized by mean susceptibility) and within-block variation is shown by 95% confidence ellipses around principal axes. These confidence ellipses are calculated using a tensor-averaging process following Jelinek (1981), assuming samples represent a homogeneous multinormal population. Parameters used to characterize AMS results are the corrected degree of anisotropy ($\boldsymbol{P_j} = \left[(\boldsymbol{\eta}_1 - \boldsymbol{\eta})^2 + (\boldsymbol{\eta}_2 - \boldsymbol{\eta})^2 + (\boldsymbol{\eta}_3 - \boldsymbol{\eta})^2\right]$; Jelinek, 1981), Shape factor ($\boldsymbol{T_j} = \left(2\boldsymbol{\eta}_2 - \boldsymbol{\eta}_1 - \boldsymbol{\eta}_3\right) / \left(\boldsymbol{\eta}_1 - \boldsymbol{\eta}_3\right)$; Jelinek, 1981), and mean susceptibility ($\boldsymbol{K_{mean}} = (\boldsymbol{K}_1 + \boldsymbol{K}_2 + \boldsymbol{K}_3)/3$; Tarling & Hrouda, 1993), where K_1, K_2, K_3 are the principal susceptibility axes and $\boldsymbol{\eta}_1$, $\boldsymbol{\eta}_2, \boldsymbol{\eta}_3$ are the natural logarithms of the respective principal susceptibility axes. All raw data processing was conducted within the SAFYR 7 program. Samples are plotted and analyzed using Anisoft 42 and Anisoft 5 software.

3.2.3. Magnetic Carrier Characterization

A series of rock magnetic and petrographic experiments were conducted to determine the type and variance of the dominant magnetic minerals across the intrusion. To assess the potential overprinting of fabrics by hydrothermal alteration, representative thin sections were taken of samples with AMS results that had no clearly defined axes and had significantly lower magnetic susceptibilities than neighboring samples (Just et al., 2004). Samples exhibiting extensive hydrothermal alteration following petrographic analyses were rejected and not taken further in data processing.

To determine the temperature dependence of susceptibility of our samples, a key diagnostic indicator of the magnetic mineralogy, cryogenic and high-temperature, low-field magnetic susceptibility experiments were conducted from a total of 14 sample sites. Representative sample off-cuts were crushed using a diamagnetic ceramic pestle and mortar, ~0.3 g of pulp underwent cryogenic and high temperature cycles using an AGICO CS-L and CS4 attached to an AGICO KLY-5A Kappabridge. Analyses were conducted in three steps: (a) cryogenic cooling of the sample to −194°C using liquid nitrogen, and warming it to room temperature; (b) heating in an argon atmosphere to 700°C and cooling back to room temperature; and (c) cooling to −194°C and warming

to room temperature. Bulk magnetic susceptibility of the sample was measured every 25 s throughout the experiment that lasted 2.5 hr in a 400 Am^{-1} peak field, 1,220 Hz peak frequency inducing field. The arising data was processed through the SAFYR 7 program. Holder corrections were performed using the Cureval 8 program.

To assess the coercivity of our samples, saturation isothermal remanent magnetism (SIRM) and backfield isothermal remanent magnetism (BIRM) were measured from the selection of representative sub-specimens that underwent temperature versus low-field magnetic susceptibility experiments. SIRM acquisition is a non-destructive method of applying a progressively larger magnetic pulse on a previously fully demagnetized sample until full magnetization is achieved (i.e., the magnetization plateaus). BIRM is subsequently achieved through stepwise remagnetization by applying a pulse in the opposite direction of the initial SIRM field. Remanent magnetism was measured using a AGICO JR-6A spinner magnetometer after each successive 5 mT pulse step. (De)magnetization was conducted using an MMPM 10 pulse magnetometer.

4. Results

4.1. Field Relationships and Petrography of the YGDC on Tuttutooq

The YGDC is exposed as two distinct dykes (50–800 m wide) on Tuttutooq that trend ENE-WSW (Figure 2b). The facies and main structural features of the YGDC are described in Koopmans et al. (2021); here we build on this work and particularly add new petrographic observations. The study area includes two YGDC sheets, which both have distinct thicker and narrower zones resulting in several lozenge-shaped sections aligned parallel to one another (Figure 3). We focus here on the southernmost sheet (Figure 3). Sharp, subvertical contacts are observed against the country rock. The outer 2–100 m of the YGDC consists of a medium-grained marginal facies, which transitions into a coarse-grained facies located toward the center of the intrusion (Koopmans et al., 2021). Several thicker zones contain isolated evolved and/or layered central pods that range from 400 × 800 m to 800 × 1,500 m in their short and long axes (Figure 3).

4.1.1. Marginal Gabbro Facies

The marginal facies of the YGDC is a medium-grained gabbro with up to 70% euhedral-subhedral plagioclase laths, euhedral olivine (10%), subhedral clinopyroxene (15%–20%) and subordinate oxides and apatite with varying crystal sizes (Figures 4a and 4b) (Koopmans et al., 2021). Magnetite forms euhedral grains as well as interstitial crystals up to 3 mm in size. Magnetite is preferentially included within olivine and aligned along olivine boundaries in the crystal framework, and appears to be the dominant magnetic mineral (5%–10%) (Figure 4a). Plag–plag–plag growth impingement textures are prevalent and tend toward 120° boundaries (Figure 4a). Horizontal melt segregate lenses up to 20 cm wide, consisting of pegmatitic plagioclase and pyroxene, are present in places and where developed align perpendicular to the strike of the dyke (Figure 4b). A *Dendritic Subfacies* occurs at some localities at the contact between the *Marginal* Facies and coarse center of the dykes, and contains dendritic plagioclase (up to 3 cm) aligned perpendicular to the strike of the dyke (Figures 4c and 4d) (Koopmans et al., 2021).

4.1.2. Homogeneous Troctolite Facies

The boundary between the marginal and homogeneous troctolite facies is sharp and lobate, with rounded blebs of the homogeneous troctolite occasionally entrained within the marginal facies (Figure 4f). The non-foliated homogeneous troctolite facies dominates the center sections of both dykes and is a coarse-grained troctolitic unit composed predominantly of cumulus euhedral plagioclase (60%–75%) and euhedral olivine (10%–25%) (Figures 4c and 4d) (Koopmans et al., 2021; Upton, 1962). Magnetite occurs as both cumulus and interstitial phases (5%–10%) and attains widths up to 5 mm (Figure 4e). Clinopyroxene occurs exclusively as an interstitial phase, and the unit defines an orthocumulate texture (Figure 4e). Minor alteration rims of maghaemite and biotite are found around some clinopyroxene and olivine crystals (Figure 4e). Growth impingement textures are prevalent around boundaries of plagioclase laths (Figure 4e). No mechanical or deformed twinning is observed, and no solid-state fabric is pervasive within the unit.

4.1.3. Foliated Troctolite Facies

In some regions of the YGDC (i.e., pods), the troctolite develops a well-defined foliation that is clearly identified in the field. Foliations consistently dip inwards, concentrically shallowing toward a horizontal point at

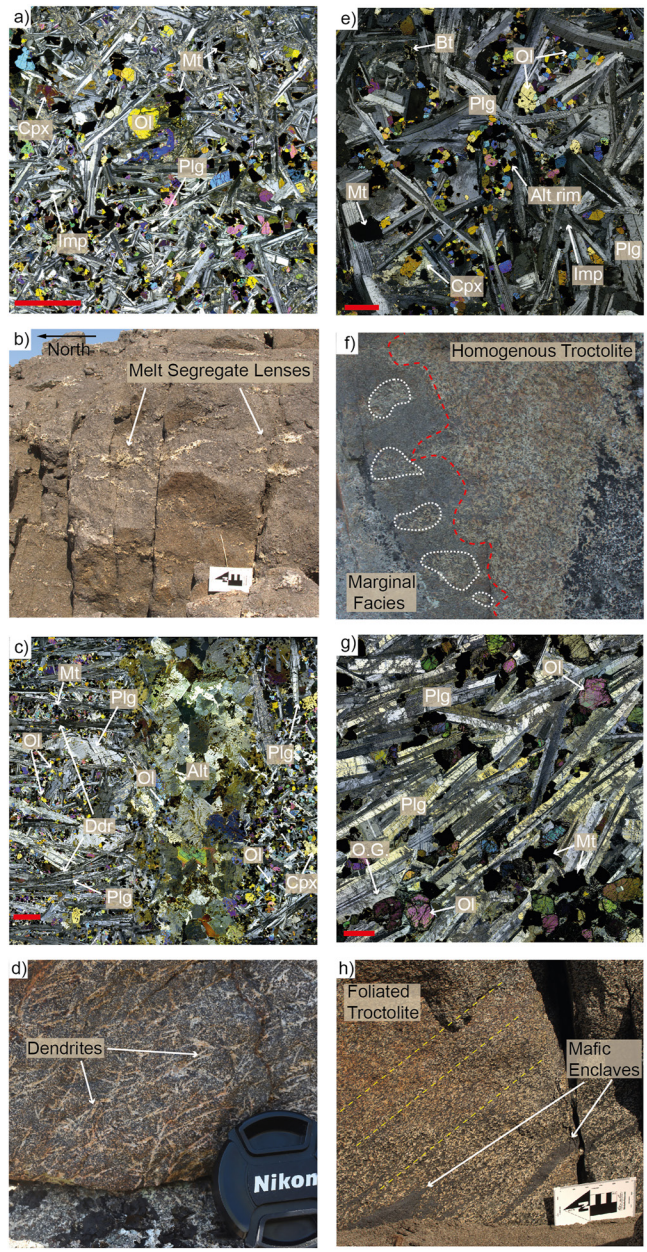

Figure 4. Petrographic and field images of all major facies in the southern Younger Giant Dyke Complex (YGDC) sheet. Red bar 2 mm wide. (a) Typical petrographic section of the Marginal Facies, showing variable crystal size and abundant impingement textures. (b) Field exposure of the Marginal Facies with elongate melt segregate lenses aligned perpendicular to the dyke-host rock contact. Note leucocratic and pegmatitic nature of the melt segregate lenses. North arrow 10 cm. (c) Petrographic image of the Homogenous Facies, showing primocrysts of plagioclase and olivine enveloped in secondary phases, with no petrographically apparent orientation. (d) Field image along the contact between the Homogenous and Marginal Facies, showing the lobate, sharp contact between the two facies. Individual rounded sections of the homogenous troctolite appear to have been enveloped by the Marginal Facies. (e) Petrographic image along the contact between the Homogenous and Dendritic Subfacies, showing the sharp and altered nature of the contact. (f) Field image showing a typical exposure of the dendritic subfacies. Lens cap 5 cm wide. (g) Typical petrographic section of the Foliated Facies indicating the clear preferential alignment of plagioclase crystals to the bottom-left of the image. Note the presence of overgrowth around primary plagioclase crystals. (h) Field image of the Foliated Facies showing the clear alignment of the plagioclase framework toward the center of the intrusion. North arrow 10 cm. Imp, impingement growth texture; Mt, magnetite; Ol, olivine; Plg, plagioclase; O.G., overgrowth texture.

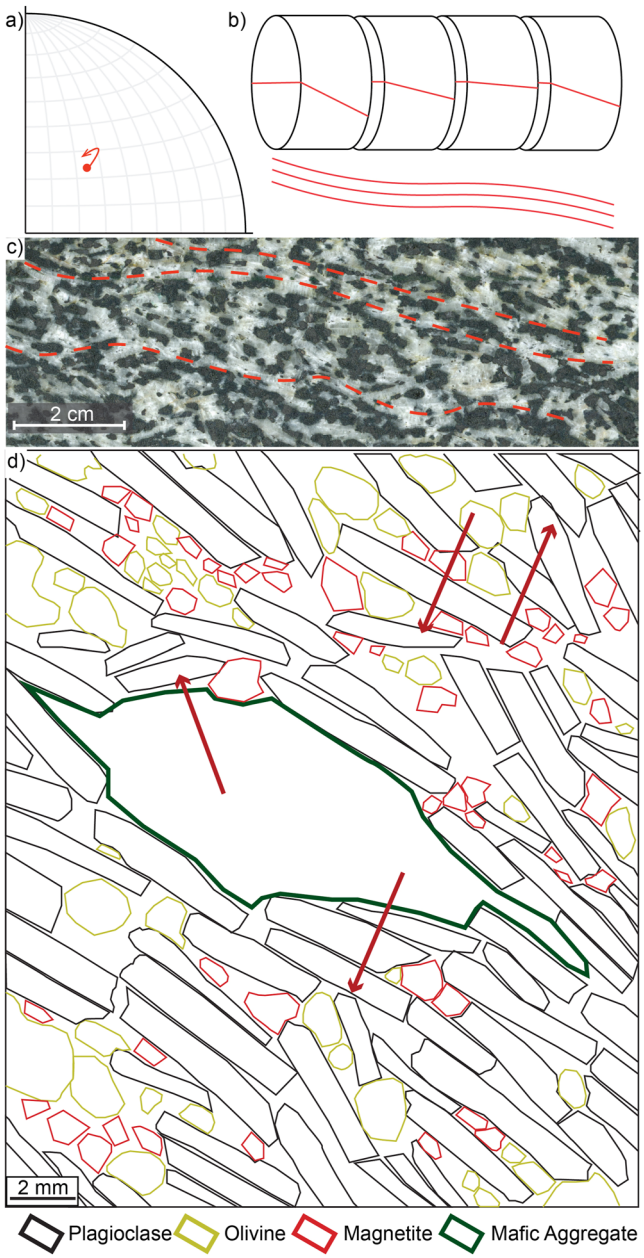

Figure 5. (a) Stereonet indicating oscillatory nature of anisotropy of magnetic susceptibility (AMS) foliation variation within sample TQ152 over 39 individual subspecimen cores. Plotted is the movement of poles to AMS foliation planes. (b) representative diagram of oscillatory AMS foliations shown in (a) along individual sample cores. The reconstructed field fabric is drawn below. (c) Block sample scan of TQ152 with ripple textures outlined in red. *Note*. the similarity in the reconstructed fabric in (b). (d) Sketch of cumulus phases in TQ143, identifying draping and imbricate textures with red arrows.

the center of the dyke, and define an ovoid morphology >1,500 m long and 700 m wide (Figure 3). No lineations were identified in the field (Koopmans et al., 2021). Cumulus euhedral plagioclase (75%–85%), euhedral olivine (5%–10%), and euhedral magnetite (5%–15%) comprise the primary phases of this facies (Figures 4g and 4h). Clinopyroxene, apatite and ilmenite occur as minor interstitial phases. Plagioclase crystals are euhedral, tabular and up to 15 mm long. There is no significant modal or crystal size variation in the *Foliated Troctolite Facies.* The framework of plagioclase, olivine and magnetite define an adcumulate texture, with only minor postcumulate plagioclase overgrowth on primary plagioclase crystals. The pervasive foliation is defined by the alignment of tabular plagioclase crystals parallel to the (010) faces, with magnetite and olivine aggregating within the crystal framework (Figure 4g). Deformation twins, dynamic recrystallization and undulose extinction are not observed within the plagioclase, and sub-grain deformation textures are not evident within the cumulus framework (Figure 4g). Tiling/imbricate structures are observed in the plagioclase framework and are aligned down-dip (Figures 5c and 5d). Plagioclase crystals also drape over other primary phases (Figure 5d). Undulose foliations, similar to ripples, occur on the cm-dm scale (similar to ripples), these trend parallel to the strike of the foliation plane and perpendicular to the tiled feldspars vergence direction (Figure 5b).

4.2. Rock Magnetic Characterization

4.2.1. Temperature-Susceptibility Experiments

Results from 14 representative temperature-susceptibility experiments show strong agreement between samples within the same facies (Figure 6). Curie temperatures (T_c) range from 480°C to 572°C, and a Verwey transition is observed in all samples between −190°C and −160°C (Figure 6a). A decrease in susceptibility temperature dependence following the Verwey transition is observed up to 20°C, indicating a relatively minor paramagnetic contribution to susceptibility at room temperature (Dunlop & Özdemir, 1997). Experiments from all facies are irreversible, with *Foliated Troctolite Facies* samples exhibiting a rise in susceptibility (except TQ055), and the *Homogeneous Troctolite Facies* and *Marginal Facies* samples exhibiting a mixture of both increase and decrease in susceptibility during cooling. The bulk susceptibility increases by ~9.1%–10.5% between the start and the end of the experiments (Figure 6a).

All *Homogeneous*, 50% of *Foliated Troctolite Facies*, and 66% of *Marginal Facies* experiment data exhibit a temporary <12% increase in susceptibility during heating between 280°C and 330°C, which may be consistent with the presence of minor titanomaghemite or iron sulphides (Figure 6a; Dunlop & Özdemir, 1997). In all samples, this increase in susceptibility between 280°C and 330°C is lost during cooling. TQ109 also indicates a magnetic phase with a Tc around −20°C is produced during the experiment (Figure 6a). The *Dendritic Subfacies* is the only sample that exhibits a considerable Hopkinson peak at 560°C during experiments (Figure 6a).

4.2.2. IRM Results

SIRM curves of representative specimens can be clustered into three distinct groups with no clear relationship to facies (Figure 6b). All samples attain saturation ($M/M_0 > 0.95$) between 100 and 170 mT. Group 1 samples exhibit

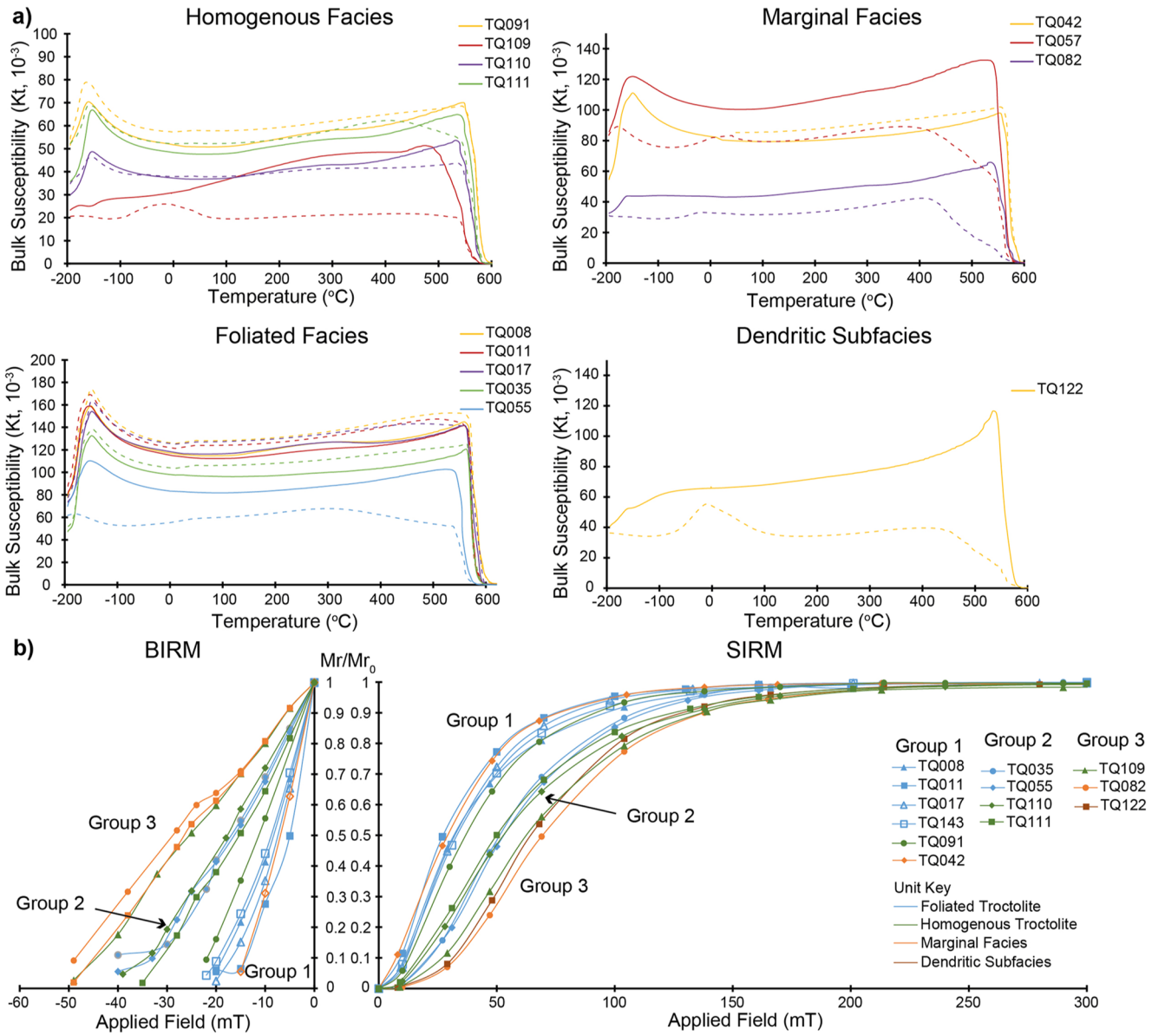

Figure 6. (a) Results of temperature-susceptibility experiments separated into individual facies. Cooling curves are in dashed lines. Note the similarity within individual facies. (b) Results of backfield IRM demagnetization (left) and IRM acquisition (right) experiments. Resultant curves can be clustered into three groups labeled Groups 1–3. Individual curves are color coded based on the corresponding facies.

near-logarithmic saturation curves, whereas group 3 samples have sigmoidal saturation curves, with an intermediate group 2 cluster. BIRM curves retain similar clustering as SIRM, with remanence canceled out by 20–50 mT (Figure 6b).

4.3. AMS Results

4.3.1. Magnetic Susceptibility

Mean magnetic susceptibility values (K_{mean}) across the intrusion average $72.4 \pm 70.7 \times 10^{-3}$ (2SD, SI units) and range from 38.1 **to** 171×10^{-3} (Figure 7). The data clearly show K_{mean} values for each facies are clustered; the *Foliated Troctolite Facies* exhibits the highest $(< 171 \times 10^{-3})$ K_{mean} values and the *Homogeneous Troctolite Facies* has the lowest average K_{mean}. Shape Factor (T_j) values range from 0.941 to −1.000 across the intrusion, with a dominance of oblate (>0) ellipsoids in the *Foliated Troctolite Facies*. Degree of anisotropy (P_j) values

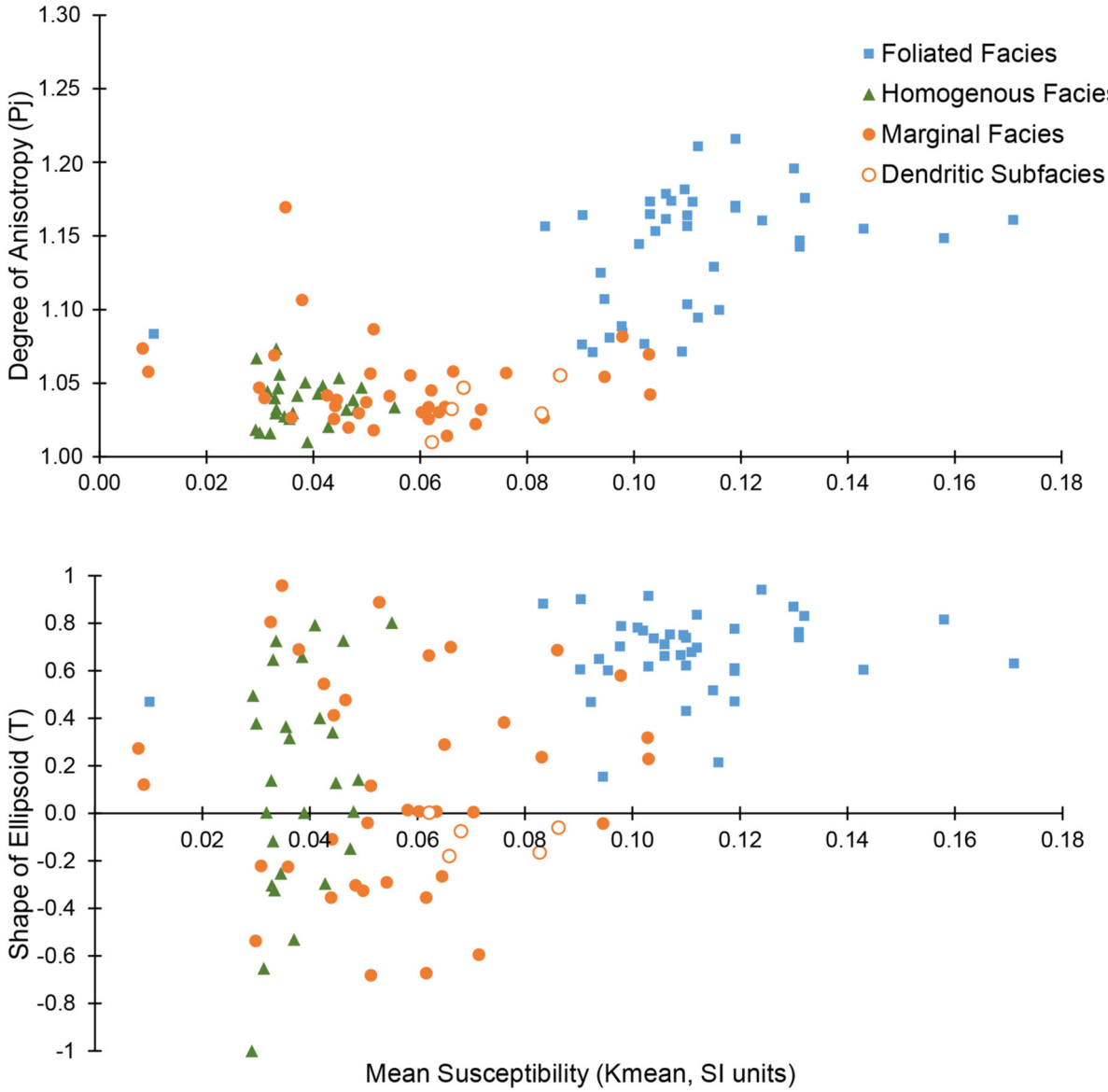

Figure 7. Degree of Anisotropy (P_j, top) and Shape of Ellipsoid (T, bottom) versus Mean Susceptibility of all anisotropy of magnetic susceptibility (AMS) samples. Top: note grouping of data from individual facies, with no apparent correlation between susceptibility and P_j values. Bottom: Both Homogenous and Marginal Facies samples are distributed evenly across prolate and oblate fabrics, with no correlation to susceptibility. Dendritic Subfacies samples are tightly clustered along the triaxial ($T = 0$) line. Foliated Facies samples are exclusively oblate, and have systematically higher susceptibility values compared to other Younger Giant Dyke Complex (YGDC) facies.

range from 1.009 to 1.515 and *Foliated Troctolite Facies* samples average higher degrees of anisotropy than other YGDC facies. There is no correlation between either T_j or P_j with K_{mean}, suggesting mineral modal differences between facies do not control the degree of anisotropy, or shape, of the magnetic fabric (Figure 7).

4.3.2. Distribution of Magnetic Fabrics

Five samples (TQ013, 033, 034, 049, 113; Table S1) from transects T1 and T5 were rejected due to anomalous AMS results with very poorly constrained, overlapping confidence ellipses of principal susceptibility directions, and 10–100 fold lower K_{mean} susceptibility values, which has been attributed to isolated hydrothermal alteration. Hydrothermal alteration was identified during petrographic analyses by the observation of weathered oxides, saussuritization of plagioclase, and pervasive chloritization. Rejected samples were not isolated to a single petrographic facies. Of the accepted data, AMS subspecimen data from individual samples show very well constrained

K_1, K_2, K_3 susceptibility axes (Figure 8) with tight confidence ellipses (average 11°), indicating AMS results of samples are internally consistent and robust, and that both a foliation and lineation can be determined from 91% of samples. Of all accepted samples, 26% AMS ellipses are dominantly prolate, and 74% are dominantly oblate (Figure 7). We note that where samples are prolate, the K_2 and K_3 axes form a slight girdle off axis to the foliation plane (e.g., TQ042, Figure 8). However, due to the tightly bound confidence ellipses of the K_3 axis, a foliation can still be obtained from these samples. Furthermore, a high degree of consistency in K_1, K_2 and K_3 orientations is observed between neighboring samples, indicating that the scale of the sampling strategy produced readily comparable data (Figure 3 and Table S1).

Foliated Troctolite Facies domains consist of oblate shape fabrics with T values ranging from 0.15 to 0.94 (Figure 7). Magnetic foliations strike concentrically around the extent of the *Foliated Troctolite Facies* zone, and foliations dip inwards between 3° and 61° and generally shallow toward the core of the *Foliated Troctolite Facies* (Figure 8a). Figure 9 calculates the difference in strike and dip between individual samples where a foliation could be observed in the field, and plots the resultant values as poles onto a stereonet. In this way, it is possible to visually compare the relationship between two fabrics. We see that the resulting poles cluster at the N and S axes of the stereonet, indicating that three magnetic foliations of the *Foliated Troctolite Facies* are aligned parallel to field observed plagioclase foliations (Figure 9). Magnetic lineations of samples with well-defined K_1 axes plunge 60°–3° down-dip of foliations (Figure 8a). Several samples (e.g., TQ152) additionally exhibit an undulation in AMS foliations forming ripple-like patterns along individual cores (Figure 5a). The undulations occur along the foliation plane (Figure 5a).

Homogeneous Troctolite Facies samples have a defined spatial distribution of shape factor across Transects 1 and 2 (Figures 8b and 8c) and magnetic lineations in both transects broadly trend ENE-WSW with sub-horizontal to shallowly inclined (<24°) plunge across the facies. The shape factor in Traverse 1 (T1) ranges from triaxial to prolate ($-1.0 < T < 0.49$) toward the center of the transect, and magnetic foliations are scattered with no apparent order or mean orientation (Figure 8b). The outer 100 m of Traverse 2 consists of oblate fabrics ($0.65 < T < 0.80$) enclosing 250 m of triaxial-dominated ($-0.32 < \mathbf{T} < 0.40$) core fabrics, and magnetic foliations dip between 75° and 12°, defining an open synformal structure across the transect (Figure 8c).

Marginal Facies samples have variable T values ($-0.68 < \mathbf{T} < 0.95$) although neighboring samples return closely comparable results (Figure 6). Lineations are typically subparallel to the strike of the intrusion walls (Figure 8). However, in samples of the *Dendritic Subfacies* ($-0.18 < T < 0$), lineations deviate toward being perpendicular to the intrusion walls, such as along the western margin of T2 (Figure 8b).

5. Discussion

5.1. Magnetic Mineralogy

5.1.1. Bulk Magnetic Mineralogy

Rock magnetic data allow the characterization of the magnetic mineralogy of the YGDC and an interrogation of the magnetic fabric data. Mean susceptibilities (K_{mean}) range from $38.1 - 171 \times 10^{-3}$ SI units across all samples (Figure 7), indicative of a ferromagnetic contribution to the bulk susceptibility (Tarling & Hrouda, 1993). The relative difference between ferro- and paramagnetic contributions to bulk magnetic susceptibility can further be analyzed by calculating the ratio of room T susceptibility and post-Tc susceptibility (Dunlop & Özdemir, 1997); our T–χ experiments indicate the ferromagnetic: paramagnetic ratio is >99.9:1 (Figure 6a) (Dunlop & Özdemir, 1997; Tarling & Hrouda, 1993). Petrographic observations also suggest the dominant ferromagnetic phase within the samples is magnetite (Figure 4). These petrographic observations are supported by T–χ heating experiments, which show Tc values between 480°C and 572°C (Figure 6a), consistent with the presence of low-Ti (0.02–0.165 X_{Ti}) titanomagnetite (Akimoto, 1962). Furthermore, this is in agreement with cryogenic T–χ experiments where a well-defined Verwey transition between −190°C and −160°C, characteristic of titanomagnetite, is observed (Figure 6a). Within the *Dendritic Subfacies*, the presence of a Hopkinson peak suggests that the blocking temperature spectrum is restricted, indicative of the presence of some single-domain magnetite (Clark & Schmidt, 1982). However, the suppression of Hopkinson peaks in all *Foliated, Homogeneous Troctolite*, and *Marginal Facies* experiments suggest the presence of single-domain magnetite is unlikely in the majority of YGDC samples (Orlický, 1990). IRM data correlate closely with T–χ heating experiment data, as saturation of all samples is achieved between 70 and 180 mT (Figure 6b), which is broadly consistent with the dominance

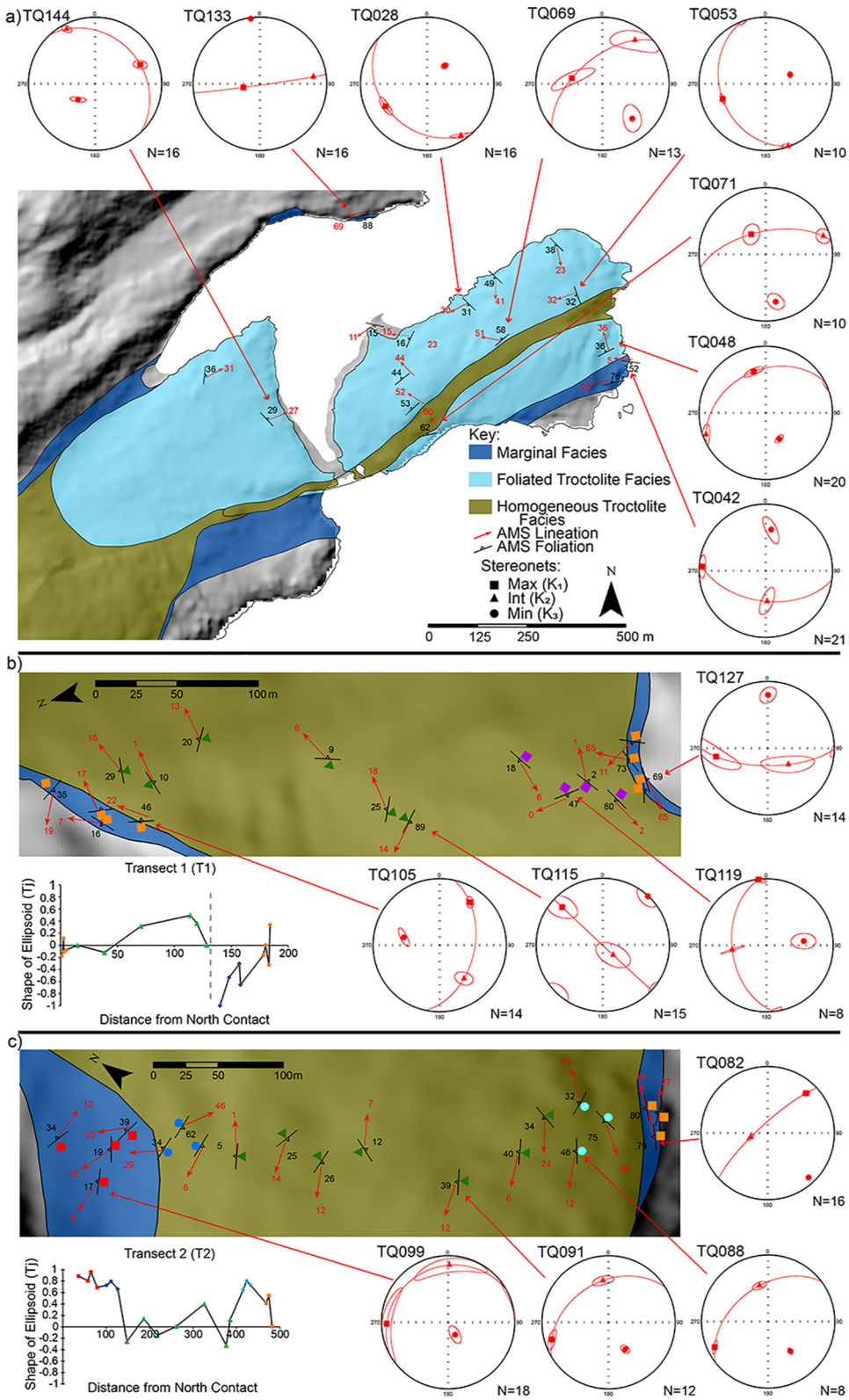
a)
TQ144
TQ133
TQ028
TQ069
TQ053
N=16
N=16
N=16
N=13
N=10
TQ071
N=10
TQ048
N=20
TQ042
N=21
Key:
Marginal Facies
Foliated Troctolite Facies
Homogeneous Troctolite Facies
AMS Lineation
AMS Foliation
Stereonets:
Max (K1)
Int (K2)
Min (K3)
N
0 125 250 500 m
b)
0 25 50 100 m
TQ127
N=14
Transect 1 (T1)
Shape of Ellipsoid (Ti)
Distance from North Contact
TQ105
TQ115
TQ119
N=14
N=15
N=8
c)
0 25 50 100m
TQ082
N=16
Transect 2 (T2)
Shape of Ellipsoid (Ti)
Distance from North Contact
TQ099
TQ091
TQ088
N=18
N=12
N=8

Figure 8.

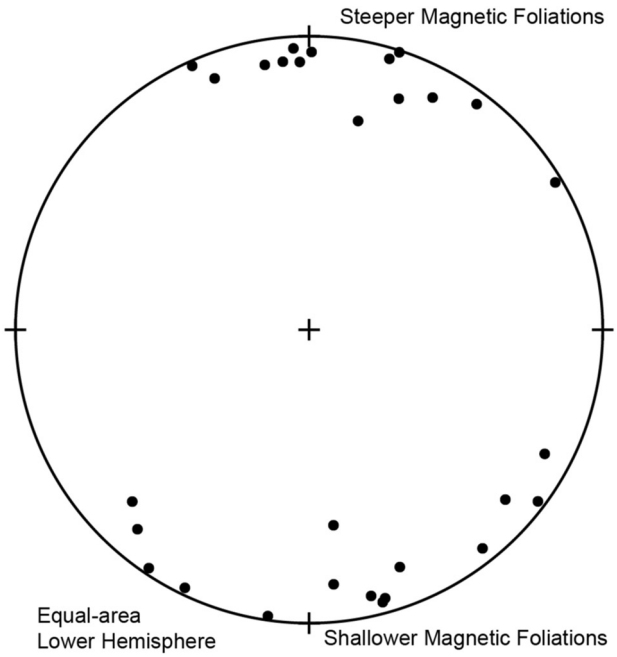

Figure 9. Stereonet plotting anisotropy of magnetic susceptibility (AMS) foliation against plagioclase foliations of Foliated Facies samples of the Eastern pod (Plotted strike = AMS strike minusplagioclase strike, plotted dip = AMS dip minusplagioclase dip). Resulting values (individual samples plotted in black dots) plotting at the top of the stereonet therefore indicate magnetic foliations are steeper within a sample, and samples at the bottom of the stereonet indicate plagioclase foliations are steeper. The clustering around the top and bottom of the stereonets indicate that AMS and plagioclase foliations are subparallel in the Eastern pod.

of multidomain (MD) magnetite with potentially a minor vortex state (VS) component (Dunlop & Özdemir, 1997). We note that *Marginal Facies* and *Homogeneous Troctolite Facies* samples exhibit both sigmoidal and logarithmic IRM saturation curves that typically saturate in fields of 100–180 mT (Figure 6b). The *Foliated Troctolite Facies* samples exhibit near-logarithmic curves and are saturated by 130 mT (Figure 6b). Whilst the variation from sigmoidal to logarithmic saturation curves are recognized, the coercivity values (70–180 mT, Figure 6b) detected are all consistent the presence of MD titanomagnetite as the dominant ferromagnetic mineral (Dunlop & Özdemir, 1997).

In rocks where the bulk susceptibility is dominated by magnetite, the bulk susceptibility is a function of the volumetric abundance of magnetite (Balsley & Buddington, 1958). Based on the bulk magnetic susceptibilities measured, we estimate the *Marginal Gabbro, Homogeneous Troctolite, and Foliated Troctolite Facies* contain ~6 vol. %, ~4 vol. %, and ~11 vol. % magnetite, respectively, which is consistent with petrographic observations (Figure 4). Integrating these data and observations support that MD magnetite dominates the bulk magnetic properties of all samples.

The broad peak around 300°C in T−χ experiments may be explained by the presence of minor titanomaghaemite alteration rims around some magnetite crystals observed in thin section (Figure 4e). Such alteration may be driven by deuteric oxidation, which drives exsolution of titanium from titanomagnetite during cooling (Dunlop & Özdemir, 1997). The 300°C peak on susceptibility heating curves is very small (<10%) and the alteration rims are an uncommon feature in petrographic analysis, implying that the titanomaghaemite likely does not negatively affect the AMS signal. Subsequent reheating during temperature-susceptibility experiments may homogenise the Fe-Ti oxides and produce new magnetite grains, explaining the higher susceptibilities and loss of the 300°C feature during cooling (Figure 6a) (Dunlop & Özdemir, 1997; Petronis et al., 2011).

5.1.2. Carrier(s) of Magnetic Anisotropy

The mineral phase dominating the bulk magnetic properties of a rock may not control its AMS if its crystals are isotropic (Biedermann & Bilardello, 2021). Tight confidence angles (averaging 15°/5°, Figure 8 and Table S1) indicate the samples have a well-defined anisotropic magnetic response. Although we have established that magnetite likely dominates the bulk magnetic signature of our samples, here we discuss whether it also likely controls the observed anisotropy.

An effective way of assessing whether magnetite is the lead contributor to AMS is by calculating the mean deviatoric susceptibility of our samples (Biedermann, 2018; Hirt & Biedermann, 2019; Jelinek, 1984). Mean deviatoric susceptibility is calculated by the following formula (after Jelinek, 1984):

$$\boldsymbol{K}' = \sqrt{\frac{(\boldsymbol{K}_1 - \boldsymbol{K}_{mean})^2 + (\boldsymbol{K}_2 - \boldsymbol{K}_{mean})^2 + (\boldsymbol{K}_3 - \boldsymbol{K}_{mean})^2}{3}}$$

Figure 8. (a): Distribution of anisotropy of magnetic susceptibility (AMS) fabrics in the Eastern pod, with representative AMS stereonets along the margins. All axes are tightly constrained and do not overlap, meaning both a lineation and foliation can be taken from AMS data. Lineations all consistently point toward the center of the Eastern pod, and foliations dip parallel to plagioclase foliations observed in the field. (b) Distribution of AMS fabrics along Transect 1 (see Figure 3 for location), the narrow section of the Western pod. AMS axes are well defined, however there is no clear structure in AMS foliations. AMS lineations are broadly contact parallel, however are not clearly aligned. Distribution of shape fabrics along Transect 1 displayed in the bottom graph. (c) Distribution of AMS fabrics along Transect 2 (see Figure 3 for location, the wider section of the Western pod. K_3 axes are very well defined, with some stretching of K_1/K_2 axes along the AMS foliation plane. AMS foliations define a synformal structure, and AMS lineations trend parallel to strike of the sheet intrusion. Distribution of shape fabrics along Transect 2 displayed in the bottom graph. Note fabrics transition from oblate to triaxial toward the center of the intrusion.

$\boldsymbol{K}'$ is thus a direct measure of the deviation of the AMS ellipsoid from a sphere whose diameter is the mean susceptibility (K_{mean}). By isolating the deviation of susceptibility from the mean susceptibility, we remove the contribution of isotropic materials from anisotropy measurements. $\boldsymbol{K}'$ is known for major paramagnetic rock forming minerals, and we can thus determine whether paramagnetic phases alone can develop the anisotropy observed in our samples (Biedermann et al., 2014, 2015, 2016). The average $\boldsymbol{K}'$ of our samples is 3.03×10^{-3}, and $\boldsymbol{K}'$ ranges from 1.59×10^{-4} to 1.16×10^{-2} (SI units). The observed values in our samples are all orders of magnitude larger than maximum values observed for pure olivine (3.10×10^{-9}, Biedermann et al., 2014), pure pyroxene (1.21×10^{-7}, Biedermann et al., 2015), and pure feldspar (1.60×10^{-9}, Biedermann et al., 2016), and therefore paramagnetic phases alone cannot produce the mean deviatoric susceptibility in our samples that contain approximately 15% olivine, 5% clinopyroxene, 70% plagioclase, and 10% magnetite. We therefore infer that the anisotropy of our samples is controlled by magnetite, which can create much larger deviatoric susceptibilities due to its AMS being grain-shape controlled (Tarling & Hrouda, 1993).

It is also important to assess whether the anisotropy caused by magnetite may be constructively or destructively affected by distribution anisotropy. Distribution anisotropy is caused by the magnetic interaction of ferromagnetic grains like titanomagnetite, and it is predicted that grain—grain interaction will occur when the ratio of mean grain size and distance between grain centers is >0.5 (Gaillot et al., 2006). Mattsson et al. (2021) shows that distribution anisotropy is likely to occur in many natural specimens due to the interaction of fine-grained, clustered magnetite that may behave as a single, larger crystal and also that the constructive and destructive impacts of distribution anisotropy can be assessed by comparing AMS fabrics to petrographically observed fabrics. In several of our samples, where clusters of magnetite are observed in thin section and AMS K_{mean} values are high, we may expect distribution anisotropy to generate competing constructive and destructive interferences due to the aggregates of titanomagnetite (e.g., Figure 4e). However, we note a very high degree of consistency between field observed fabrics and the orientation of the K_1 and K_3 AMS axes in such samples (Figure 9). Additionally, P_j values are low relative to samples where a field observed fabric is very subtle, whereas a marked increase in P_j is expected when distribution anisotropy is present in samples with weak petrographic fabrics (Figure 7). We interpret these observations as evidence that textural distribution anisotropy does impact the AMS fabric in YGDC samples.

Due to the presence of abundant cumulus magnetite, alongside petrographic observations of interstitial magnetite bound by the framework of the primary silicate phases, and a lack of evidence for distribution anisotropy, we infer that the shape anisotropy of magnetite controls the AMS in our samples, which conforms to any present petrographic alignment. The dominance of MD magnetite in bulk susceptibility experiments additionally suggest that the AMS is parallel to the shape anisotropy of magnetite; we therefore consider the magnetic fabrics are probably normal, and representative of a true petrographic rock fabrics (Ferré, 2002).

5.2. Formation of YGDC Pods

5.2.1. Sheet Segments

The contact geometry of sheet intrusions can provide valuable information regarding the emplacement of individual dykes or sills (e.g., Magee et al., 2019). For example, the presence of steps and other connector forms (e.g., broken bridges), which can occur on the centimeter—tens of meter scale, indicate many sheet intrusions were emplaced as a series of individual segments instead of a single planar body (e.g., Healy et al., 2018; Hutton, 2009; Magee, Muirhead, et al., 2016; Nicholson & Pollard, 1985; Schofield, Heaton, et al., 2012). Continued magma input enables these segments to inflate and coalesce into a continuous sheet intrusion (e.g., Hutton, 2009; Martin et al., 2019; Schofield, Heaton, et al., 2012). Furthermore, the long axes of element connectors parallels the their propagation direction (Magee et al., 2019). Detailed field mapping of the southern YGDC contacts indicate several ovoid segments occur that are up to 2,500 m long and 800 m wide, and are separated by narrower (100–300 m wide) sections (Figure 10). Individual segments are orientated parallel to the strike of the dyke (ENE-WSW) and the long axis of their connecting sections appears to be sub-vertical (Figure 10). Facies contacts between *Marginal Gabbro, Homogeneous Troctolite and Foliated Troctolite Facies* occur concentrically within these individual ovoid dyke segments (Koopmans et al., 2021). We interpret this contact geometry to reflect the vertical emplacement of the YGDC as a series of isolated segments that later coalesced to form a single sub-vertical sheet intrusion (Figure 10).

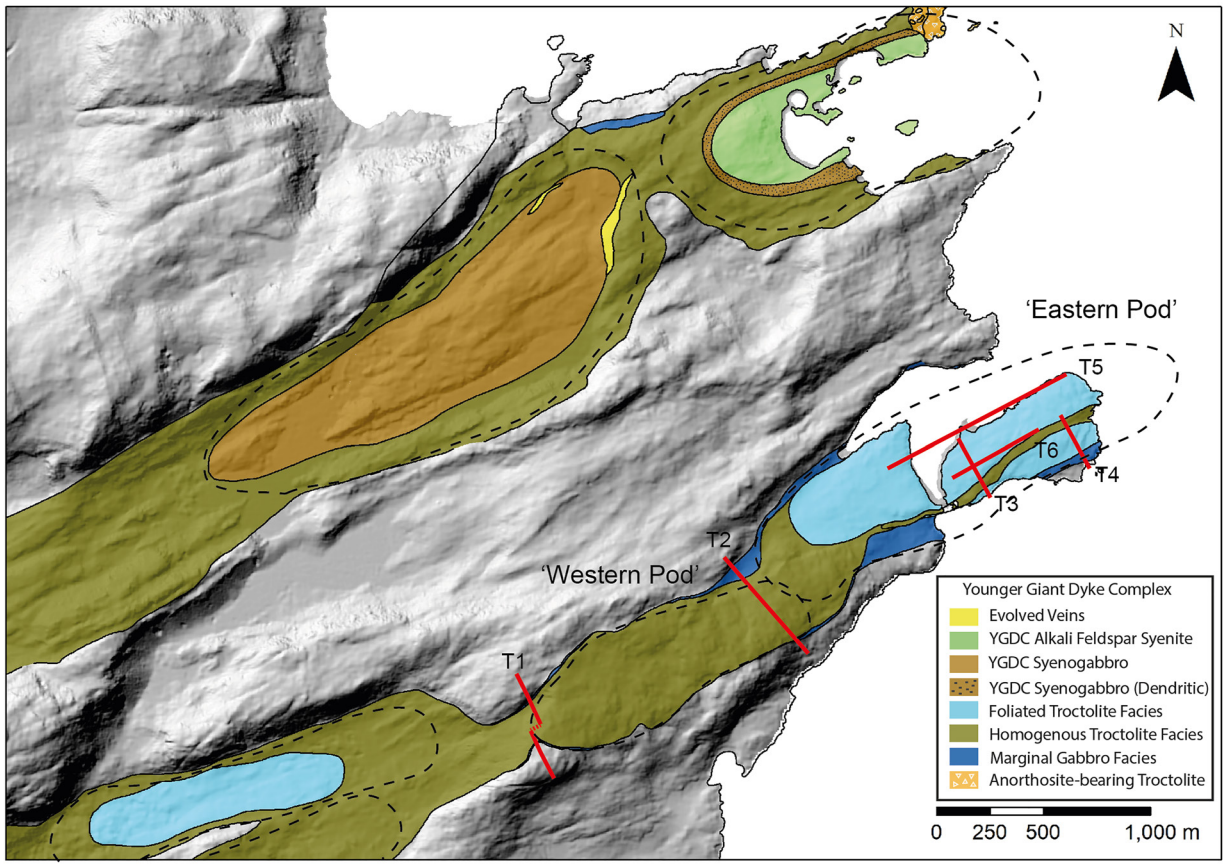

Figure 10. Map of YGDC exposures in NE Tuttutooq, with individual dyke element locations inferred with black dashed lines. Sample transects are labeled and traced in red. Note how individual ovoid elements, connected by thinner zones, are clearly identifiable in map view.

5.2.2. Origin of Fabrics in the Eastern Pod

In studies of other intrusions, magnetic lineations and foliations have been interpreted to reflect contrasting magma flow processes (e.g., Knight & Walker, 1988; Maes et al., 2007; O'Driscoll et al., 2007). For example, flow-induced crystal alignment can occur during several stages of sheet intrusion development: (a) initial emplacement, forming imbricate fabrics sub-parallel and immediately adjacent to intrusion margins (Ferré & Marsh, 2002; Knight & Walker, 1988); (b) dynamic post-emplacement processes (e.g., convection) (Holness et al., 2019; McBirney & Nicolas, 1997; Selkin et al., 2014); (c) late-stage subsidence and/or slumping of an unconsolidated crystal mush (Higgins, 1991; McBirney & Nicolas, 1997; O'Driscoll et al., 2007, 2008; VanTongeren et al., 2015); or (d) viscous compaction or simple shear in the sub-magmatic or solid state arising from magnetic or tectonic stress (Bolle et al., 2000; McCarthy et al., 2015; Nicolas, 1992; Paterson et al., 1998; Wiebe & Collins, 1998). The criteria to distinguish syn-magmatic (i.e., emplacement, dynamic, or mush) from post-magmatic (i.e., sub-solidus or tectonic) fabrics are outlined by Nicolas (1992) and Paterson et al. (1998): a well-defined alignment of largely undeformed euhedral primocrystic igneous minerals surrounded by anhedral interstitial material indicate that syn-magmatic processes are preserved, whereas the presence of significant plastic strain and/or grain boundary migration suggests a post-magmatic overprint has occurred. Maes et al. (2007) additionally suggest that high degrees of anisotropy (P_j) would support the presence of post-magmatic compaction, as primary flow fabrics do not consistently attain $\mathbf{P_j} > 1.2$.

Key features of the eastern pod (Figure 10) are that it consists primarily of the *Foliated Troctolite Facies*, AMS K_1 axes (i.e., magnetic lineations) define a radial pattern that plunge toward the center of the pod, and the K_3 axes define planes (i.e., magnetic foliations) that subparallel visible foliations (Figure 9) and dip toward the center of the pod (Figure 7). Petrographic sections of the *Foliated Troctolite Facies* display an adcumulate texture, with clear boundaries between euhedral crystals (Figure 4g). Cumulus plagioclase crystals define an aligned

framework and display no evidence of crystal plastic deformation, and no sub-grain textures are observed within cumulus olivine or magnetite crystals (Figure 4g). Based on these petrographic observations and the definitions outlined by Nicolas (1992) and Paterson et al. (1998), we consider the *Foliated Troctolite Facies* in the Eastern pod records syn-magmatic processes, such that the magnetic lineations likely reflect magma flow parallel to the K_1 axis (Meurer & Boudreau, 1998a; O'Driscoll et al., 2008).

Structures resembling ripples are observed in the Eastern pod and show low-angle undulose magnetic foliations (Figure 5) that trend perpendicular to AMS K_1 axes, which could support our interpretation that AMS K_1 axes reflect magmatic state flow. The presence of such possible pseudo-sedimentary structures are classically attributed to dynamic processes occurring at the liquid-mush boundary (Irvine, 1980; McBirney & Nicolas, 1997; Meurer & Boudreau, 1998a, 1998b). We also note that tabular plagioclase crystals in the *Foliated Troctolite Facies* exhibit imbricate/tiling structures, and drape over other cumulus phases (Figure 5b), which is typically attributed to flow in magmatic settings (Holness et al., 2019; Nicolas, 1992; Tex, 1969); a similar fabric is preserved in AMS foliations, which are imbricated subparallel to the plagioclase framework (Figure 5a). The imbrication observed between plagioclase and AMS foliations may be driven by the difference in aspect ratio between plagioclase and magnetite, as the tabular shape of plagioclase enhances its ability to be kept at an angle to flow direction (Nicolas, 1992; Tex, 1969). Given the apparent presence of ripple-like structures and crystal imbrication, both of which are pseudo-sedimentary flow indicators, we infer the foliated troctolite facies captures sorting and flow at the liquid-mush interface (Meurer & Boudreau, 1998a; Tex, 1969). Formation of the Eastern Pod Foliated Troctolite at a liquid-mush interface is further supported by the uniform crystal size of the cumulus phases, as this is consistent with hydrodynamic sorting (Holness et al., 2019). Subsequent deformation of the flow fabric due to crystal mush processes is unlikely, as no macroscopic slump-folds or wrapping of tabular crystals around euhedral crystals has been observed (cf. O'Driscoll et al., 2008). Overall, the above evidence suggests the foliation observed in the *Foliated Troctolite Facies* formed due to syn-magmatic flow at the liquid-mush interface (Figure 11b). Owing to the concentric and inward inclination of plagioclase foliations, tiling structures, and AMS fabrics in the Eastern Pod, magma flow is interpreted to have had a flow vector toward the center of the pod from all directions. We suggest that the magmatic state radial petrographic fabric pattern, tiled feldspars, and ovoid facies geometry could be generated by a density driven convection cell that was controlled by the shape of the dyke element (Figure 11). Convection has been inferred to occur in several tabular intrusions (Holness, Farr, et al., 2017; Holness, Neufeld, et al., 2017; Irvine, 1980; Selkin et al., 2014), and is thought to dominate the magmatic evolution of dykes (Holness, Neufeld, et al., 2017). Within convective systems, deposition is restricted to the viscous boundary layer at the liquid-mush interface, as fluid velocities become negligible in this region (Holness, Farr, et al., 2017). This is in good agreement with our observations in the Eastern pod, where processes of hydrodynamic sorting and settling are inferred to lead to the development of the *Foliated Troctolite Facies* (Figure 11b).

The location of crystal nucleation and growth in a layered intrusion is classically thought to be along the walls of the intrusion (Irvine, 1980; Meurer & Boudreau, 1998b; Nicolas, 1992). If this was the case in the YGDC, the *Marginal Facies* should source the crystals deposited at the base of the convective system. However, as the *Marginal Facies* of the intrusion have a distinctly different crystal population (finer crystal sizes, lower vol. % plagioclase and olivine) to what is observed in the Foliated Troctolite Facies of the Eastern pod, we consider it unlikely that the crystals now located at core of the Eastern pod originally crystallized along the walls of the dyke (Figures 4a vs. 3e, 11b). The sharp boundary observed in the field and in AMS shape (T) values between the central and marginal zones of the Eastern pod instead suggests a change in crystallization regime across the boundary. Whereas the center of the Eastern pod (consisting of the *Foliated Troctolite Facies*) formed through convective settling, with crystal nucleation within the convective cell, we suggest the *Marginal Facies* formed through in-situ crystallization of a propagating wall mush. The propagation of the wall mush is thought to occur simultaneously, though independent of, convection occurring in the center of the pod (Figure 11b). In this way, any evidence of emplacement fabrics during unidirectional flow, commonly found as imbricates at the margins of sheet intrusions (Knight & Walker, 1988; Magee, O'Driscoll, et al., 2016; L. Tauxe et al., 1998), are likely overprinted, as suggested by Holness, Farr, et al. (2017). The resulting petrographic and AMS fabrics are therefore a result of post-emplacement processes, once unidirectional flow has ceased. The protracted cooling period (10^2–10^4 yrs, Cawthorn, 2012; Holness, Neufeld, et al., 2017; Martin et al., 1987) of an intrusion of this size would promote the presence of post-emplacement processes, such as the initiation of convection, as is inferred to occur in the Eastern pod. The simultaneous crystallization of the *Marginal Facies* and the central troctolite facies

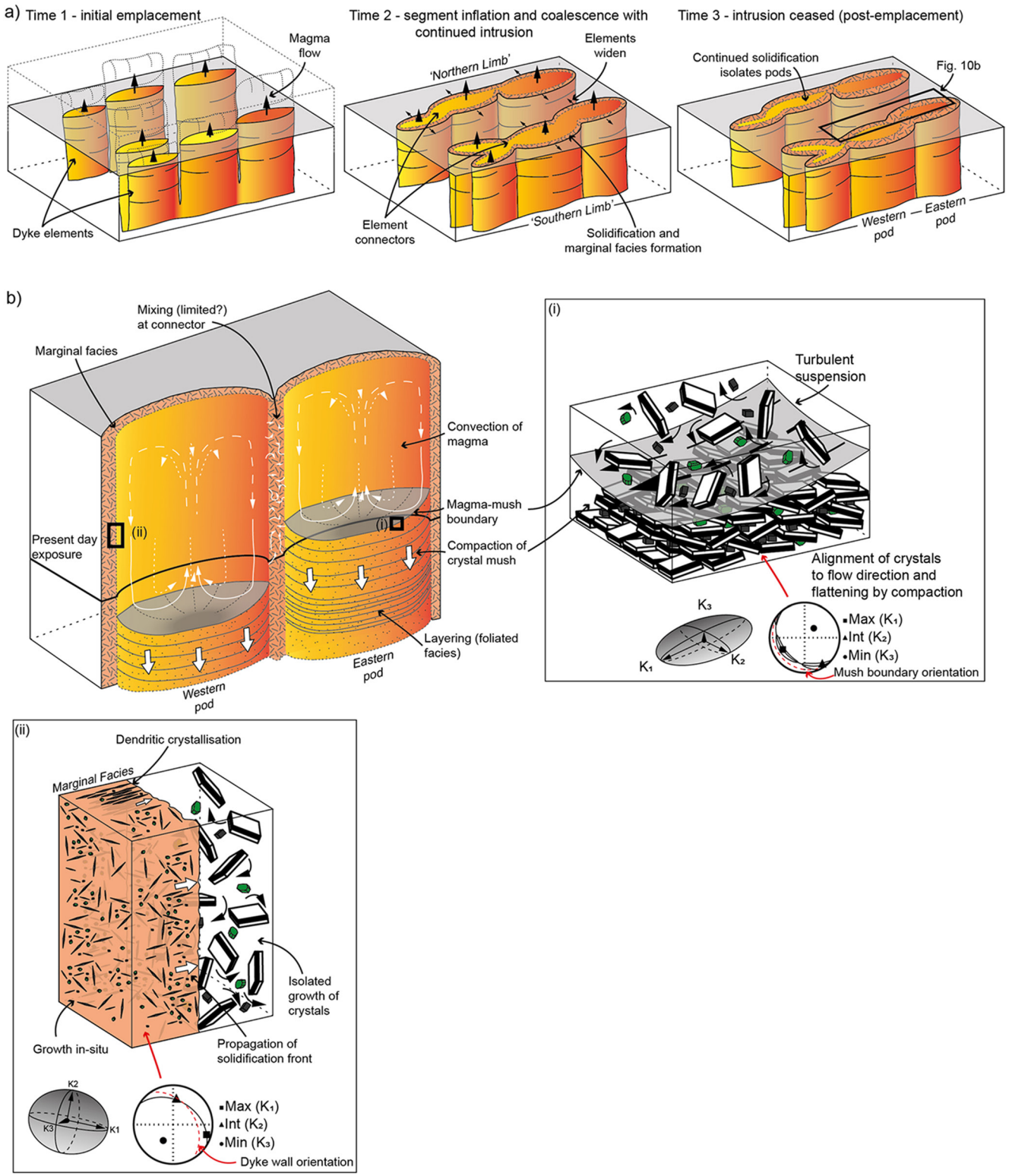

Figure 11.

can explain the mingling textures observed at the boundary between the two facies (Figure 4f). In-situ crystallization is in agreement with a low degree of anisotropy of the AMS data (Figure 7), which suggests crystallization occurred under low-stress conditions. Additionally, the presence of abundant impingement textures and variable

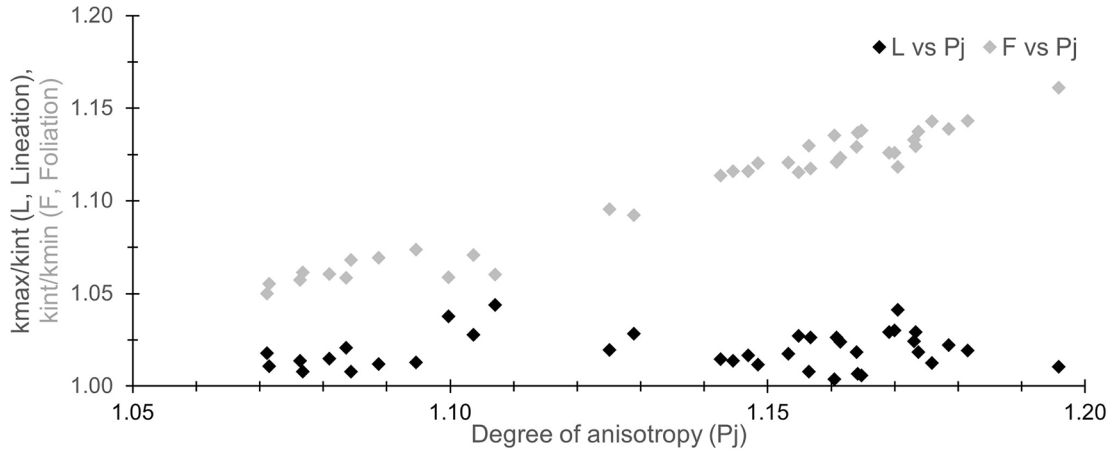

Figure 12. Results of plotting the degree of foliation (F) and lineation (L) against the degree of anisotropy (P_j) (method modified from Selkin et al. (2014)). There is a clear correlation between the degree of foliation and P_j, with no apparent change in lineation, suggesting a component of compaction occurred in the Eastern pod.

crystal size (Figure 4a) has been suggested to be a product of in-situ crystallization (Holness et al., 2019). Local expressions of the *Dendritic Subfacies* further support this interpretation, as dendritic crystallization (Figures 4c and 4d) is attributed to rapid crystallization due to undercooling of melt saturated with the dendritic phase (Chalmers, 1964; Dawson & Hawthorne, 1973; Donaldson, 1982; Vukmanovic et al., 2013). Overall, our model of two separate crystallization regimes within the YGDC is broadly consistent with that of Holness, Farr, et al. (2017) who, based on plagioclase aspect ratio, long axis length, and clinopyroxene-plagioclase-plagioclase dihedral angle data, suggested that crystallization within dykes involves an inwards propagating wall mush and a convecting core. However, whereas Holness, Farr, et al. (2017) showed an invariance in plagioclase crystal size occurs across all dyke widths because convection dominated crystallization across the full width of the dyke, the YGDC preserves a finer grained *Marginal Facies* zone, which is distinctly different to the coarser core of the intrusion (Figure 11). We therefore suggest that in sufficiently wide dykes, wall mush propagation can impede convection, such that a separation of zones occurs.

5.2.3. Post-Depositional Compaction in the Eastern Pod

Post-depositional compaction due to a growing mush zone is expected to alter the original AMS deposition fabric below a convection system (Meurer & Boudreau, 1998b; Selkin et al., 2014). We note that AMS P_j values of the *Foliated Troctolite Facies* in the Eastern pod average 1.142 and has a maximum of 1.216 (Figure 6), which straddles the threshold between maximum values expected for flow-related anisotropy and the minimum values expected for post emplacement magmatic state overprinting (Maes et al., 2007). To test the presence of compaction in the Eastern pod, we follow the method outlined by Selkin et al. (2014), who modeled the effect of compaction and stretching on an originally anisotropic AMS fabric. By comparing the difference in the change of the degree of lineation (L, K_1/K_2) and degree of foliation (F, K_2/K_3) with increasing degree of anisotropy (P_j), one can assess the presence of possible overprinting fabrics such as compaction or slumping (Selkin et al., 2014). For example, the process of compaction would lead to a positive correlation between the degree of foliation and P_j whilst the degree of lineation remains constant, and slumping would lead a positive correlation between the degree of lineation and the P_j with a constant degree of foliation (Selkin et al., 2014). Samples of *Foliated Troctolite Facies* in the Eastern pod show a clear increase in the degree of foliation with P_j, with no appreciable increase in the degree of lineation (Figure 12); this is consistent with modeled compaction related overprint

Figure 11. Schematic diagram of Younger Giant Dyke Complex (YGDC) evolution through time. (a) Time stepped evolution of YGDC from individual dyke elements to final magmatic events, leading to the stepped exposures visible from map view. Location of (b) marked by black rectangle in time step 3. (b) Schematic diagram of magmatic processes occurring once emplacement has ceased. Deposition at the magma-mush boundary at the bottom of the convective cell leads to the growth of the layered mush pile. As the pile grows, the overburden leads to gravitational compaction of the lower mush pile. Locations of insets (i) and (ii) marked in black squares. (i) Schematic diagram of formation of layered mush pile below convecting magma. Crystal alignment is parallel to magmatic flow directions. A representative AMS ellipsoid and corresponding stereonet for this process is drawn below. The AMS ellipsoid is parallel to the direction of flow, and flattened parallel to the magma-mush boundary. (ii) Schematic diagram of interaction between the solidification front and convecting core of the YGDC. The representative AMS fabric is more triaxial than in (i) due to weaker processes of alignment occurring.

(Selkin et al., 2014). We therefore interpret this result to indicate minor compaction occurred due to mafic crystal loading at the within the magma mush (Figure 11b).

5.2.4. Adjacent Dyke Element Variation

To assess the validity of our interpretation that individual dyke segments may have controlled geometrically distinct convection cells, we consider the adjacent Western pod (Figure 10). Transects across the Western Pod show magnetic foliations define a synformal geometry across the width of the intrusion that is most apparent in wider sections of the pod. The presence of the synformal structure ceases toward the western edge of the pod where the dyke narrows before expanding into an adjacent dyke segment (Figures 8b and 8c). Primary phases in the *Homogeneous Troctolite Facies* core of the Western pod are euhedral, indicating crystal growth was likely uninhibited during the initial phases of crystallization. Additionally, plagioclase primocrysts display synneusis, forming aggregates aligned along crystallization planes, which indicates crystallization occurred in a liquid-rich environment when crystal growth along preferred axes was likely uninhibited (Holness et al., 2019; Holness, Farr, et al., 2017). Given the similar dyke contact relationships, pod geometries and petrographic textures observed in the Eastern and Western pods (Figures 9 and 10), we suggest that convection may also have occurred in the Western Pod, but that the *Homogeneous Troctolite Facies* formed higher up in the convective system. Whereas the synformal AMS structure in the Eastern pod is observed in the cumulus framework, AMS fabrics in the Western pod are not corroborated by a synonymous petrographic fabric. Hydrodynamic sorting is therefore not likely to have occurred at this structural level of the western pod, as we observe no development of pseudo-sedimentary structures. We also note that the *Homogeneous* and *Foliated Troctolite Facies* exhibit very similar crystal modes and sizes, which suggest that crystals deposited at the base of the convecting cell in the Eastern pod (dominantly *Foliated Troctolite Facies*) may have been sourced from a structurally higher level of the same cell. The structurally higher level of a convective cell would be analogous to the current exposure level of the Western Pod (dominantly *Homogeneous Troctolite Facies*) (Figure 11).

The interface between individual dyke element pods is defined by weaker fabrics with irregular orientations (Figure 8a). The increase in fabric heterogeneity could be tied to multiple processes such as structural overprinting (Borradaile & Jackson, 2004), late-stage fluid or magma remobilization (Martin et al., 2019), or limited mixing as segments coalesce (Magee et al., 2013; Magee, O'Driscoll, et al., 2016). The proximity of the fabrics in T1 (Figures 7a and 9) to a connector between segments may indicate that the lack of alignment is caused by the interaction between competing convection cells, or perhaps partial overprinting of magma transport fabrics due to excess magma overpressure relaxation after the termination of the magma supply (Figure 11). Further work is required to better understand the nature of the irregular orientations. Nevertheless, the data shows that even after sheet segments coalesce, the cores of individual segments remain isolated. Individual segments in large dykes may thus behave independently during crystallization, with only minimal influence of magma mixing.

6. Conclusions

An integrated approach of field mapping, petrographic studies and AMS analyses enabled the development of a model for the multi-stage magmatic evolution of the YGDC, where high density transects were pivotal to providing a robust interpretation of the AMS results. Field observations revealed the presence of clearly distinguishable dyke segments aligned along strike which subsequently coalesced during inflation of the intrusion. Critically, AMS data indicate that mixing between segments was likely limited, suggesting that individual dyke segments experienced isolated magmatic histories. This observation therefore enables cross-sections of sheet intrusions to preserve different magmatic structural levels, providing a unique insight into the three-dimensional evolution of large vertical intrusions.

We conclude that the Eastern and Western pods of the YGDC on Tuttutooq represent different structural levels of adjacent density driven convective cells. Whereas the Western pod is representative of the core of a convective cell, the Eastern pod preserves the interaction of the convecting magma and underlying mush, forming a well-defined foliation due to deposition and hydrodynamic sorting atop a growing mush layer. Importantly, the original dyke element geometry imparted a structural control on the distribution of magma crystallization regimes within the YGDC. Finally, convection in the YGDC appears to have been vigorous enough to overcome the propagation of the solidification front, separating the crystallization at the walls from the core of the intrusion.

Data Availability Statement

All rock magnetic data, including AMS, temperature-susceptibility, and induced remanent magnetism experiments, used for this study are available for use under a CC BY 4.0 license in a Mendeley Data repository via doi: http://doi.org/10.17632/dwwxzh9xjt.2.

Acknowledgments
The mapping and field data presented in this manuscript are the result of a field expedition to Tuttutooq in 2019. The expedition was funded by the Mining Institute of Scotland Trust, the Institute of Materials, Minerals and Mining, the Society of Economic Geologists Hickok-Radford Fund (SRG_19-59), the Edinburgh Geological Society, the Augustine Courtauld trust and the Scott Polar Research Institute. Two detailed and insightful reviews by A. R. Biedermann and E. Zanella greatly improved the quality of the manuscript. We thank Rory Changleng, Lucy Mathieson, Robert Webster and Alasdair Murphy for their support during the field expedition. We also thank Prof. Brian Upton and Prof. Adrian Finch for their endless insight into this region of the Gardar Province.

References

Akimoto, S. (1962). Magnetic properties of FeO-Fe_2O_3-TiO_2 system as a basis of rock magnetism. *Proceedings on the International Conference on Magnetism and Crystallography*, *17*(Supplement B1), 706–710.

Andersen, T. (1997). Age and petrogenesis of the Qassiarsuk carbonatite-alkaline silicate volcanic complex in the Gardar rift, South Greenland. *Mineralogical Magazine*, *61*(407), 499–513. https://doi.org/10.1180/minmag.1997.061.407.03

Balsley, J. R., & Buddington, A. F. (1958). Iron-titanium oxide minerals, rocks, and aero-magnetic anomalies of the Adirondack area, New York. *Economic Geology*, *53*(7), 777–805. https://doi.org/10.2113/gsecongeo.53.7.777

Biedermann, A., & Bilardello, D. (2021). Misconceptions in magnetic fabric interpretation. *IRM Quarterly*, *31*(3), 1–18.

Biedermann, A. R. (2018). Magnetic anisotropy in single crystals: A review. *Geosciences (Switzerland)*, *8*(8), 20–28. https://doi.org/10.3390/geosciences8080302

Biedermann, A. R., Kunze, K., & Hirt, A. M. (2018). Interpreting magnetic fabrics in amphibole-bearing rocks. *Tectonophysics*, *722*, 566–576. https://doi.org/10.1016/J.TECTO.2017.11.033

Biedermann, A. R., Pettke, T., Angel, R. J., & Hirt, A. M. (2016). Anisotropy of magnetic susceptibility in alkali feldspar and plagioclase. *Geophysical Journal International*, *205*(1), 479–489. https://doi.org/10.1093/gji/ggw042

Biedermann, A. R., Pettke, T., Bender Koch, C., & Hirt, A. M. (2015). Magnetic anisotropy in clinopyroxene and orthopyroxene single crystals. *Journal of Geophysical Research: Solid Earth*, *120*(3), 1431–1451. https://doi.org/10.1002/2014JB011678

Biedermann, A. R., Pettke, T., Reusser, E., & Hirt, A. M. (2014). Anisotropy of magnetic susceptibility in natural olivine single crystals. *Geochemistry, Geophysics, Geosystems*, *15*(7), 3051–3065. https://doi.org/10.1002/2014GC005386

Bolle, O., Diot, H., & Duchesne, J. C. (2000). Magnetic fabric and deformation in charnockitic igneous rocks of the Bjerkreim-Sokndal layered intrusion (Rogaland, Southwest Norway). *Journal of Structural Geology*, *22*(5), 647–667. https://doi.org/10.1016/S0191-8141(99)00183-2

Borradaile, G. J., & Jackson, M. (2004). *Anisotropy of Magnetic susceptibility (AMS): Magnetic petrofabrics of deformed rocks* (Vol. 238, pp. 299–360). Geological Society Special Publication. https://doi.org/10.1144/GSL.SP.2004.238.01.18

Cashman, K. V., Stephen, R., & Sparks, J. (2013). How volcanoes work: A 25 year perspective. *Bulletin of the Geological Society of America*, *125*(5–6), 664–690. https://doi.org/10.1130/B30720.1

Cawthorn, R. G. (2012). Multiple Sills or a layered intrusion? *Time to Decide*, *115*, 283–290. https://doi.org/10.2113/gssajg.115.3.283

Chadwick, B., Erfurt, P., Frisch, T., Frith, R. A., Garde, A. A., Schonwandt, H. K., et al. (1994). Sinistral transpression and hydrothermal activity during emplacement of the Early Proterozoic Julianehab Batholith, Ketilidian orogenic belt, South Greenland. In *Re-interpretation of aspects of Ketilidian geology*. (pp. 5–22).

Chalmers, B. (1964). *Principles of solidification*. Wiley.

Cheadle, M. J., & Gee, J. S. (2017). Quantitative textural insights into the formation of gabbro in mafic Intrusions. *Elements*, *13*(6), 409–414. https://doi.org/10.2138/gselements.13.6.409

Clark, D. A., & Schmidt, P. W. (1982). Theoretical analysis of thermomagnetic properties, low-temperature hysteresis and domain structure of titanomagnetites. *Physics of the Earth and Planetary Interiors*, *30*(4), 300–316. https://doi.org/10.1016/0031-9201(82)90029-2

Dawson, J., & Hawthorne, J. (1973). Magmatic sedimentation and carbonatitic differentiation in kimberlite sills at Benfontein, South Africa. *Journal of Geological Society (London)*, *129*, 61–85. https://doi.org/10.1144/gsjgs.129.1.0061

Donaldson, C. H. (1982). Origin of some of the Rhum harrisite by segregation of intercumulus liquid. *Mineralogical Magazine*, *45*(337), 201–209. https://doi.org/10.1180/minmag.1982.045.337.23

Dunlop, D. J., & Özdemir, Ö. (1997). *Rock magnetism*. Cambridge University Press. https://doi.org/10.1017/cbo9780511612794

Ferré, E. C. (2002). Theoretical models of intermediate and inverse AMS fabrics. *Geophysical Research Letters*, *29*(7), 31-31–31-4. https://doi.org/10.1029/2001GL014367

Ferré, E. C., & Marsh, J. S. (2002). Magma flow inferred from AMS fabrics in a layered mafic sill Insizwa, South Africa. *Tectonophysics*, *354*, 1–23.

Gaillot, P., de Saint-Blanquat, M., & Bouchez, J. L. (2006). Effects of magnetic interactions in anisotropy of magnetic susceptibility: Models, experiments and implications for igneous rock fabrics quantification. *Tectonophysics*, *418*(1–2), 3–19. https://doi.org/10.1016/j.tecto.2005.12.010

Garde, A. A., Hamilton, M. A., Chadwick, B., Grocott, J., & McCaffrey, K. J. W. (2002). The Ketilidian orogen of South Greenland: Geochronology, tectonics, magmatism, and fore-arc accretion during Palaeoproterozoic oblique convergence. *Canadian Journal of Earth Sciences*, *39*(5), 765–793. https://doi.org/10.1139/e02-026

Healy, D., Rizzo, R. E., Du, M., Farrell, N. J. C., Hole, M. J., & Muirhead, D. (2018). Field evidence for the lateral emplacement of igneous dykes: Implications for 3D mechanical models and the plumbing beneath fissure eruptions. *Volcanica*, *1*(2), 85–105. https://doi.org/10.30909/vol.01.02.85105

Higgins, M. D. (1991). The origin of laminated and massive anorthosite, Sept Iles layered intrusion, Quebec, Canada. *Contributions to Mineralogy and Petrology*, *106*, 340–354. https://doi.org/10.1007/BF00324562

Higgins, M. D. (2006). Quantitative textural measurements in igneous and metamorphic petrology. *Quantitative Textural Measurements in Igneous and Metamorphic Petrology*, *9780521847827*, 1–265. https://doi.org/10.1017/CBO9780511535574

Hirt, A. M., & Biedermann, A. R. (2019). Preferred orientation of ferromagnetic phases in rock-forming minerals: Insights from magnetic anisotropy of single crystals. *Canadian Journal of Earth Sciences*, *56*(9), 994–1001. https://doi.org/10.1139/cjes-2018-0172

Holness, M. B., & Humphreys, M. C. S. (2003). The Traigh Bhan na Sgurra Sill, Isle of Mull: Flow localization in a major magma conduit. *Journal of Petrology*, *44*(11), 1961–1976. https://doi.org/10.1093/petrology/egg066

Holness, M. B., Farr, R., & Neufeld, J. A. (2017). Crystal settling and convection in the Shiant Isles Main Sill. *Contributions to Mineralogy and Petrology*, *172*(1), 1–25. https://doi.org/10.1007/s00410-016-1325-x

Holness, M. B., Neufeld, J. A., Gilbert, A. J., & Macdonald, R. (2017). Orientation of tabular mafic intrusions controls convective vigour and crystallization style. *Journal of Petrology*, *58*(10), 2035–2053. https://doi.org/10.1093/petrology/egx081

Holness, M. B., Stock, M. J., & Geist, D. (2019). Magma chambers versus mush zones: Constraining the architecture of sub-volcanic plumbing systems from microstructural analysis of crystalline enclaves. *Philosophical Transactions of the Royal Society A: Mathematical, Physical & Engineering Sciences*, *377*(2139), 20180006. https://doi.org/10.1098/rsta.2018.0006

Hutton, D. H. W. (2009). Insights into magmatism in volcanic margins: Bridge structures and a new mechanism of basic sill emplacement—Theron Mountains, Antarctica. *Petroleum Geoscience*, *15*(3), 269–278. https://doi.org/10.1144/1354-079309-841

Irvine, T. (1980). Magmatic density currents and cumulus processes. *American Journal of Science*, *280*(A), 1–58.

Jelinek, V. (1981). Characterization of the magnetic fabric of rocks. *Tectonophysics*, *79*(3–4), T63–T67. https://doi.org/10.1016/0040-1951(81)90110-4

Jelinek, V. (1984). On a mixed quadratic invariant of the magnetic susceptibility tensor. *Journal of Geophysics*, *56*(1), 58–60.

Just, J., Kontny, A., De Wall, H., Hirt, A. M., & Martín-Hernández, F. (2004). *Development of magnetic fabrics during hydrothermal alteration in the Soultz-Sous-Forêts Granite from the EPS-1 Borehole, Upper Rhine Graben* (Vol. 238, pp. 509–526). Geological Society Special Publication. https://doi.org/10.1144/GSL.SP.2004.238.01.26

Khan, M. A. (1962). The anisotropy of magnetic susceptibility of some igneous and metamorphic rocks. *Journal of Geophysical Research*, *67*(7), 2873–2885. https://doi.org/10.1029/JZ067I007P02873

Knight, M. D., & Walker, G. P. L. (1988). Magma flow directions in dikes of the Koolau Complex, Oahu, determined from magnetic fabric studies. *Journal of Geophysical Research*, *93*(B5), 4301–4319. https://doi.org/10.1029/JB093iB05p04301

Koopmans, L., Webster, R. A., Changleng, R., Mathieson, L., Murphy, A. J., Finch, A. A., & McCarthy, W. (2021). New insights from field observations of the Younger giant dyke complex and mafic lamprophyres of the Gardar Province on Tuttutooq island, South Greenland. *GEUS Bulletin*, *47*. https://doi.org/10.34194/geusb.v47.6526

Maes, S. M., Tikoff, B., Ferré, E. C., Brown, P. E., & Miller, J. D. (2007). The Sonju Lake layered intrusion, northeast Minnesota: Internal structure and emplacement history inferred from magnetic fabrics. *Precambrian Research*, *157*(1–4), 269–288. https://doi.org/10.1016/j.precamres.2007.02.021

Magee, C., Muirhead, J., Schofield, N., Walker, R. J., Galland, O., Holford, S., et al. (2019). Structural signatures of igneous sheet intrusion propagation. *Journal of Structural Geology*, *125*, 148–154. https://doi.org/10.1016/j.jsg.2018.07.010

Magee, C., Muirhead, J. D., Karvelas, A., Holford, S. P., Jackson, C. A. L., Bastow, I. D., et al. (2016). Lateral magma flow in mafic sill complexes. *Geosphere*, *12*(3), 809–841. https://doi.org/10.1130/GES01256.1

Magee, C., O'Driscoll, B., Petronis, M. S., & Stevenson, C. T. E. (2016). Three-dimensional magma flow dynamics within subvolcanic sheet intrusions. *Geosphere*, *12*(3), 842–866. https://doi.org/10.1130/GES01270.1

Magee, C., O'driscoll, B., Petronis, M. S., Stevenson, C. T. E., Clay, P. L., & Gertisser, R. (2013). Magma rheology variations in sheet intrusions of the Ardnamurchan Central Complex (Scotland) inferred from gabbro inclusion characteristics. *Journal of Petrology*, *54*(1), 75–102. https://doi.org/10.1093/petrology/egs064

Magee, C., Stevenson, C., O'Driscoll, B., Schofield, N., & McDermott, K. (2012). An alternative emplacement model for the classic Ardnamurchan cone sheet swarm, NW Scotland, involving lateral magma supply via regional dykes. *Journal of Structural Geology*, *43*, 73–91. https://doi.org/10.1016/j.jsg.2012.08.004

Martin, D., Griffiths, R. W., & Campbell, I. H. (1987). Compositional and thermal convection in magma chambers. *Contributions to Mineralogy and Petrology*, *96*(4), 465–475. https://doi.org/10.1007/bf01166691

Martin, S. A., Kavanagh, J. L., Biggin, A. J., & Utley, J. E. P. (2019). The origin and evolution of magnetic fabrics in mafic sills. *Frontiers of Earth Science*, *7*(April), 1–23. https://doi.org/10.3389/feart.2019.00064

Mattsson, T., Petri, B., Almqvist, B., McCarthy, W., Burchardt, S., Palma, J. O., et al. (2021). Decrypting magnetic fabrics (AMS, AARM, AIRM) through the analysis of mineral shape fabrics and distribution anisotropy. *Journal of Geophysical Research: Solid Earth*, *126*(6), e2021JB021895. https://doi.org/10.1029/2021JB021895

McBirney, A. R., & Nicolas, A. (1997). The Skaergaard layered series. Part II. Magmatic flow and dynamic layering. *Journal of Petrology*, *38*(5), 569–580. https://doi.org/10.1093/petroj/38.5.569

McCarthy, W., Petronis, M. S., Reavy, R. J., & Stevenson, C. T. (2015). Distinguishing diapirs from inflated plutons: An integrated rock magnetic fabric and structural study on the Roundstone Pluton, western Ireland. *Journal of the Geological Society*, *172*(5), 550–565. https://doi.org/10.1144/jgs2014-067

Meurer, W. P., & Boudreau, A. E. (1998a). Compaction of igneous cumulates part I: Geochemical consequences for cumulates and liquid fractionation trends1. *Journal of Geology*, *106*(3), 281–292. https://doi.org/10.1086/516022

Meurer, W. P., & Boudreau, A. E. (1998b). Compaction of igneous cumulates part II: Compaction and the development of igneous foliations1. *Journal of Geology*, *106*(3), 293–304. https://doi.org/10.1086/516023

Nicholson, R., & Pollard, D. D. (1985). Dilation and linkage of echelon cracks. *Journal of Structural Geology*, *7*(5), 583–590. https://doi.org/10.1016/0191-8141(85)90030-6

Nicolas, A. (1992). Kinematics in magmatic rocks with special reference to gabbros. *Journal of Petrology*, *33*, 891–915. https://doi.org/10.1093/petrology/33.4.891

O'Driscoll, B., Ferré, E. C., Stevenson, C. T. E., Magee, C., & Magee, C. (2015). *The significance of magnetic fabric in layered mafic-ultramafic intrusions* (pp. 295–329). Springer GeologySpringer. https://doi.org/10.1007/978-94-017-9652-1_7

O'Driscoll, B., Hargraves, R. B., Emeleus, C. H., Troll, V. R., Donaldson, C. H., & Reavy, R. J. (2007). Magmatic lineations inferred from anisotropy of magnetic susceptibility fabrics in units 8, 9, and 10 of the Rum Eastern Layered Series, NW Scotland. *Lithos*, *98*(1–4), 27–44. https://doi.org/10.1016/j.lithos.2007.01.009

O'Driscoll, B., Stevenson, C. T. E., & Troll, V. R. (2008). Mineral lamination development in layered gabbros of the british palaeogene igneous province: A combined anisotropy of magnetic susceptibility, quantitative textural and mineral chemistry study. *Journal of Petrology*, *49*(6), 1187–1221. https://doi.org/10.1093/petrology/egn022

Orlický, O. (1990). Detection of magnetic carriers in rocks: Results of susceptibility changes in powdered rock samples induced by temperature. *Physics of the Earth and Planetary Interiors*, *63*(1–2), 66–70. https://doi.org/10.1016/0031-9201(90)90060-B

Paterson, S. R., Fowler, T. K., Schmidt, K. L., Yoshinobu, A. S., Yuan, E. S., & Miller, R. B. (1998). Interpreting magmatic fabric patterns in plutons. *Lithos*, *44*(1–2), 53–82. https://doi.org/10.1016/S0024-4937(98)00022-X

Petronis, M. S., O'Driscoll, B., & Lindline, J. (2011). Late stage oxide growth associated with hydrothermal alteration of the Western Granite, Isle of Rum, NW Scotland. *Geochemistry, Geophysics, Geosystems*, *12*(1), 1001–n. https://doi.org/10.1029/2010GC003246

Rochette, P., Jackson, M., & Aubourg, C. (1992). Rock magnetism and the interpretation OF magnetic susceptibility. *Reviews of Geophysics*, *30*(3), 209–226. https://doi.org/10.1029/92RG00733

Schofield, N. J., Brown, D. J., Magee, C., & Stevenson, C. T. (2012). Sill morphology and comparison of brittle and non-brittle emplacement mechanisms. *Journal of the Geological Society*, *169*(2), 127–141. https://doi.org/10.1144/0016-76492011-078

Schofield, N. J., Heaton, L., Holford, S. P., Archer, S. G., Jackson, C. A. L., & Jolley, D. W. (2012). Seismic imaging of "broken bridges": Linking seismic to outcrop-scale investigations of intrusive magma lobes. *Journal of the Geological Society*, *169*(4), 421–426. https://doi.org/10.1144/0016-76492011-150

Selkin, P. A., Gee, J. S., & Meurer, W. P. (2014). Magnetic anisotropy as a tracer of crystal accumulation and transport, Middle Banded series, Stillwater Complex, Montana. *Tectonophysics*, *629*(C), 123–137. https://doi.org/10.1016/j.tecto.2014.03.028

Tarling, D. H., & Hrouda, F. (1993). *The magnetic anisotropy of rocks*. London: Chapman & Hall.

Tauxe, L. (1998). *Paleomagnetic principles and practice* (p. 299).

Tauxe, L., Gee, J. S., & Staudigel, H. (1998). Flow directions in dikes from anisotropy of magnetic susceptibility data: The bootstrap way. *Journal of Geophysical Research: Solid Earth*, *103*(8), 17775–17790. https://doi.org/10.1029/98jb01077

Tex, E. D. (1969). Origin of ultramafic rocks, their tectonic setting and history: A contribution to the discussion of the paper "the origin of ultramafic and ultrabasic rocks" by P.J. Wyllie. *Tectonophysics*, *7*(5–6), 457–488. https://doi.org/10.1016/0040-1951(69)90016-X

Upton, B. G. J. (1962). Geology of Tugtutoq and neighbouring islands, South Greenland, Part 1. *Meddelelser Om Gronland*, *169*(8), 1–60. https://doi.org/10.34194/bullggu.v34.6568

Upton, B. G. J. (2013). Tectono-magmatic evolution of the younger Gardar southern rift, South Greenland. *Geological Survey of Denmark and Greenland (GEUS) Bulletin*, *29*(29), 1–24. https://doi.org/10.34194/geusb.v29.4692

Upton, B. G. J., & Emeleus, C. H. (1987). Mid-Proterozoic alkaline magmatism in southern Greenland: The Gardar province. *Geological Society Special Publication*, *30*(May 2007), 449–471. https://doi.org/10.1144/GSL.SP.1987.030.01.22

Upton, B. G. J., Emeleus, C. H., Heaman, L. M., Goodenough, K. M., & Finch, A. A. (2003). Magmatism of the mid-Proterozoic Gardar Province, South Greenland: Chronology, petrogenesis and geological setting. *Lithos*, *68*(1–2), 43–65. https://doi.org/10.1016/S0024-4937(03)00030-6

van Kranendonk, M. J., St-Onge, M. R., & Henderson, J. R. (1993). Paleoproterozoic tectonic assembly of Northeast Laurentia through multiple indentations. *Precambrian Research*, *63*(3–4), 325–347. https://doi.org/10.1016/0301-9268(93)90039-5

VanTongeren, J. A., Hirth, G., & Kelemen, P. B. (2015). Constraints on the accretion of the gabbroic lower oceanic crust from plagioclase lattice preferred orientation in the Samail ophiolite. *Earth and Planetary Science Letters*, *427*, 249–261. https://doi.org/10.1016/j.epsl.2015.07.001

Vukmanovic, Z., Barnes, S. J., Reddy, S. M., Godel, B., & Fiorentini, M. L. (2013). Morphology and microstructure of chromite crystals in chromitites from the Merensky Reef (Bushveld Complex, South Africa). *Contributions to Mineralogy and Petrology*, *165*(6), 1031–1050. https://doi.org/10.1007/s00410-012-0846-1

Wiebe, R. A., & Collins, W. J. (1998). Depositional features and stratigraphic sections in granitic plutons: Implications for the emplacement and crystallization of granitic magma. *Journal of Structural Geology*, *20*(9–10), 1273–1289. https://doi.org/10.1016/S0191-8141(98)00059-5

Wing-Fatt, L., & Stacey, F. D. (1966). Magnetic anisotropy of laboratory materials in which magma flow is simulated. *Pure and Applied Geophysics*, *6464*(11), 78–80. https://doi.org/10.1007/BF00875533